RMT focal plane sensitivity to seismic network geometry and faulting style

Kendra L. Johnson,[1,2] Gavin P. Hayes,[1] Robert B. Herrmann,[3] Harley M. Benz,[1]
Dan E. McNamara[1] and Eric Bergman[4]

[1]*National Earthquake Information Center, U.S. Geological Survey, Golden, CO 80401, USA. E-mail: kejohnso@mines.edu*
[2]*Department of Geophysics, Colorado School of Mines, Golden, CO 80401, USA*
[3]*Department of Earth and Atmospheric Sciences, Saint Louis University, St. Louis, MO 63108, USA*
[4]*Global Seismological Services, Golden, CO 80401, USA*

SUMMARY

Modern tectonic studies often use regional moment tensors (RMTs) to interpret the seismo-tectonic framework of an earthquake or earthquake sequence; however, despite extensive use, little existing work addresses RMT parameter uncertainty. Here, we quantify how network geometry and faulting style affect RMT sensitivity. We examine how data-model fits change with fault plane geometry (strike and dip) for varying station configurations. We calculate the relative data fit for incrementally varying geometries about a best-fitting solution, applying our workflow to real and synthetic seismograms for both real and hypothetical station distributions and earthquakes. Initially, we conduct purely observational tests, computing RMTs from synthetic seismograms for hypothetical earthquakes and a series of well-behaved network geometries. We then incorporate real data and station distributions from the International Maule Aftershock Deployment (IMAD), which recorded aftershocks of the 2010 M_W 8.8 Maule earthquake, and a set of regional stations capturing the ongoing earthquake sequence in Oklahoma and southern Kansas. We consider RMTs computed under three scenarios: (1) real seismic records selected for high data quality; (2) synthetic seismic records with noise computed for the observed source-station pairings and (3) synthetic seismic records with noise computed for all possible station-source pairings. To assess RMT sensitivity for each test, we observe the 'fit falloff', which portrays how relative fit changes when strike or dip varies incrementally; we then derive the ranges of acceptable strikes and dips by identifying the span of solutions with relative fits larger than 90 per cent of the best fit. For the azimuthally incomplete IMAD network, Scenario 3 best constrains fault geometry, with average ranges of 45° and 31° for strike and dip, respectively. In Oklahoma, Scenario 3 best constrains fault dip with an average range of 46°; however, strike is best constrained by Scenario 1, with a range of 26°. We draw two main conclusions from this study. (1) Station distribution impacts our ability to constrain RMTs using waveform time-series; however, in some tectonic settings, faulting style also plays a significant role and (2) increasing station density and data quantity (both the number of stations and the number of individual channels) does not necessarily improve RMT constraint. These results may be useful when organizing future seismic deployments (e.g. by concentrating stations in alignment with anticipated nodal planes), and in computing RMTs, either by guiding a more rigorous data selection process for input data or informing variable weighting among the selected data (e.g. by eliminating the transverse component when strike-slip mechanisms are expected).

Key words: Time-series analysis; Earthquake source observations; Seismicity and tectonics.

1 INTRODUCTION

Regional seismic networks detect earthquakes that may otherwise be too small to be systematically detected by global networks. Often, temporary regional networks are deployed in locations of heightened seismotectonic interest. Following recent large and high-impact earthquakes, collaborative efforts have rapidly deployed temporary networks of dense instrumentation to collect data on post-earthquake earth processes and seismic effects. For example, following the 2010 M_W 8.8 Maule earthquake offshore central Chile, a multinational effort organized and deployed >160-instrument temporary seismic network to monitor the aftershock sequence (Beck *et al*. 2014). Groups of temporary regional seismometers have also been established in areas experiencing an increase in regional seismicity levels. For example, heightened seismicity in Oklahoma and southern Kansas, USA, since late 2009 prompted the deployment of seismometers by several organizations, combining with the existing permanent networks to total over 100 monitoring stations in the region (McNamara *et al*. 2015a). In both cases, the seismic records of regional events recorded by such instruments can be used to compute regional moment tensors (RMTs).

RMTs have been used extensively to interpret regional seismotectonic framework (e.g. Giardini *et al*. 1993; Ritsema & Lay 1993; Romanowicz *et al*. 1993; Braunmiller *et al*. 1994, 2002; Nabelek & Xia 1995; and more recently Ristau *et al*. 2007; Herrmann *et al*. 2011a; Hayes *et al*. 2013), but despite frequent use, comparatively little work has addressed the uncertainties of RMT solutions. Past studies confirm that the moment tensor inversion is sensitive to the configuration of available seismic stations. Early studies of RMT uncertainty assessed single-station RMT inversions using body and surface waves (Dufumier & Cara 1995; Dufumier 1996, respectively), determining that this station configuration is highly unstable and that at a minimum inversions should use data from three stations separated by 60°. They also found that stations within 30° of each other have very similar spectra, and that some contrasting focal mechanisms (pure strike-slip or 45° dip-slip) are indistinguishable without 3-component spectra. Ford *et al*. (2009) established that RMT solution sensitivity varies with network geometry. Pesicek *et al*. (2012) demonstrated how an RMT solution changes when different station combinations are used in the inversion. Šílený *et al*. (1996) showed how the confidence level and per cent double–couple of a solution depend on whether stations are evenly distributed throughout the focal sphere or densely clustered in one region.

Some previous work has also placed quantitative bounds on the resolution of RMT parameters, such as fault plane strike and dip. Robinson & Cheung (2010) tested the solution space about their best-fitting moment tensor for the 2003 Tokachi-Oki earthquake and its aftershocks. They found instabilities in some moment tensor components for strike-slip earthquakes on steeply dipping faults, but not for dip-slip earthquakes on shallowly dipping faults. Stich *et al*. (2003) found poor dip and rake resolution for strike-slip earthquakes on the Iberian Peninsula, and attributed this to similar radiation patterns over a broad parameter space. They also observed poorly constrained strike for earthquakes with poor azimuthal coverage. More recently, Zahradník & Custódio (2012) converted uncertainties for a derived moment tensor into strike, dip and rake uncertainties, focusing on double-couple uncertainty, with or without waveforms. They found that shallow earthquakes are more easily resolved than deep earthquakes; more stations improve resolution for deep earthquakes; azimuthal coverage often helps, but for shallow sources can be compensated for by station density; and that single station inversions are possible when low frequencies are included. Michele

et al. (2014) used the same method to show that for earthquakes in southern Italy, focal mechanism resolution was better in areas with high station density as opposed to central within the station distribution.

Here, we attempt to further quantify how network geometry and faulting style affect RMT sensitivity. We examine how data-model fits change with fault plane geometry for varying station configurations. We evaluate the solution constraint in RMT inversions using real and synthetic seismograms for real and hypothetical regional seismic station distributions and earthquakes. For each case, we compute a best-fitting solution, defined as the solution with the highest data-model fit for observed and predicted waveform time-series, and then calculate the relative data misfit for solutions of incrementally varying strike and dip within a large range surrounding the best-fitting solution. We then use information on change in relative fit over the solution space to determine the model sensitivity to strike or dip variations.

Our preliminary tests are purely observational, computing RMTs from synthetic seismograms for two hypothetical earthquakes and a series of well-behaved network geometries. We then incorporate data from real regional networks: (1) for the International Maule Aftershock Deployment (IMAD), which recorded aftershocks of the 2010 M_W 8.8 Maule earthquake and (2) for a set of regional stations capturing the ongoing earthquake sequence in Oklahoma and southern Kansas. We compare the change in data-model fit—computed in a least-squares sense (Herrmann *et al*. 2011a)—within the solution space—defined as the 'fit fall-off'—for the real data to that produced using synthetic seismograms for the same earthquake-station pairings. This allows us to quantify how our RMT sensitivities are affected by data quality. Last, we model the 'real' earthquakes at all deployed stations in the respective networks, again using synthetic data, and test the capability of a seismic network's geometry independent of the temporal variability in that geometry and of data quality, to assess the best accuracy we can hope to achieve for different networks and faulting styles. We compute ranges of acceptable strike that span 9° to >71°, and ranges of acceptable dip that span 20° to >71°. These ranges are in many cases symmetric, but sometimes are asymmetric about the best-fitting solution. Asymmetry is not considered in computing the range; that is, the reported ranges represent the full extent of acceptable solutions but the best-fitting solution is not necessarily in the centre of the range. We then address the station distribution characteristics and fault geometry parameters that impact the significant interevent variability of these recovered RMT sensitivities. Finally, we consider the implications for studies in which RMTs inform seismotectonic interpretation, and the implications for regional seismic network deployment.

2 DATA

This section describes the input data for the RMT inversions. For both test cases, we use velocity waveforms recorded by regional broad-band stations within 600 km of the relocated hypocentres of Hayes *et al*. (2013) and McNamara *et al*. (2015a).

2.1 International Maule aftershock deployment (IMAD)

Following the 2010 February 27 M_W 8.8 Maule earthquake, an international effort deployed a 164-instrument temporary seismic network, including 91 broad-band stations, 48 short period stations, and 25 accelerometers, over a ∼700 × ∼150 km region surrounding the on land extent of the rupture (Fig. 1). This regional network,
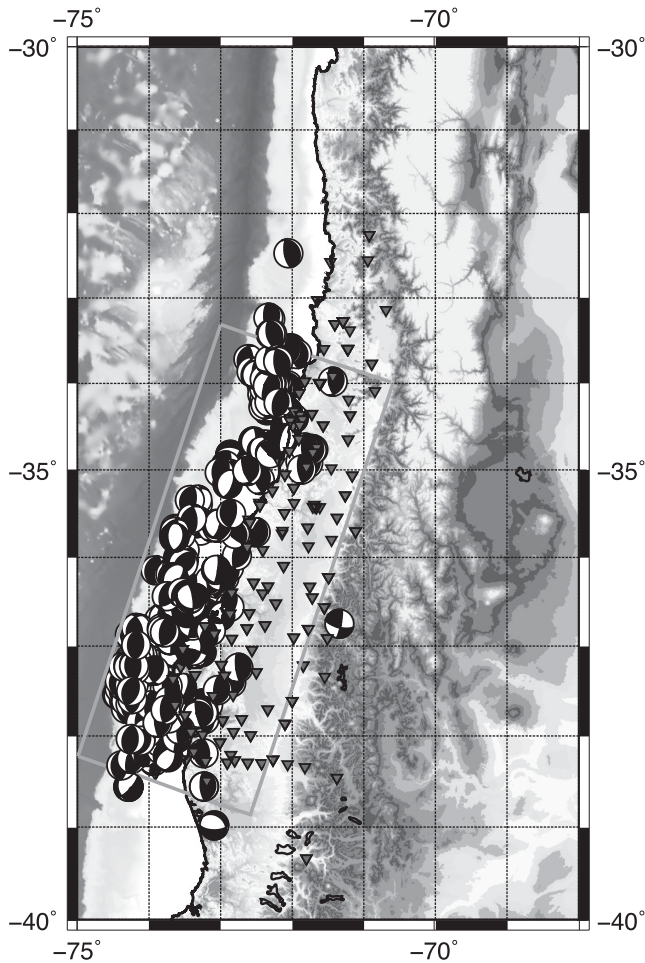
Figure 1. IMAD temporary network (inverted triangles) and focal mechanisms for earthquakes with repeatable RMTs in the Maule test case. Thick black line traces the Chilean coast.

called the International Maule Aftershock Deployment (IMAD) temporary network, recorded ∼30 000 aftershocks over the ∼9 months following the main shock (Beck *et al.* 2014). Because the subduction zone and coast trend roughly linearly in the north–south direction, and because the seismogenic zone is mostly offshore, all seismometers were deployed east (towards the downdip extent) of the main shock and most aftershocks.

We collated the available data for all events into our own waveform server. We selected from up to 133 three-component broadband and short-period stations for each event. Note that this number is less than the 164 deployed stations because a few consistently faulty stations were eliminated. There were no events for which we included data traces from all 133 stations, partially because epicentral variation among earthquakes means different sets of stations fall within 600 km of the epicentre and in part because not all stations recorded high quality data for all earthquakes.

2.2 Oklahoma networks

Because of its intracontinental setting, Oklahoma offers the ability to surround a high-seismicity zone with more evenly distributed seismometers than was possible with the IMAD deployment. Over the past several years, temporary and permanent seismic networks—which combined provide azimuthally complete coverage of the

region—have detected thousands of small to moderate-sized earthquakes in Oklahoma and southern Kansas.

The regionally dense seismic stations (Fig. 7, McNamara *et al.* 2015a) allowed detection and RMT computation for these earthquakes. Due to a sudden increase in seismicity rate in Oklahoma, the Oklahoma Geologic Survey deployed 12 new seismic stations in 2012. The USGS also added stations to their network during the time frame of this study. Two additional temporary deployments also detected events. In November 2011, three $M_W \geq 5.0$ earthquakes near Prague, Oklahoma prompted a several-station local deployment by the University of Oklahoma and the Program for Array Seismic Studies of the Continental Listhosphere Rapid Array Mobiliazation Program (PASSCAL RAMP), providing improved station coverage at close distances. These stations recorded the latter two events as well as many aftershocks and remained in place through May 2012. The beginning of our study period also overlaps with the passage of the EarthScope Project USArray Transportable Array (TA) through eastern Oklahoma and states directly to the east. Three other existing deployments—the Cooperative New Madrid, Arkansas and Central and Eastern U.S. Seismic Networks—complete the available data set for this test case. In addition to more complete azimuthal coverage, the Oklahoma earthquakes were recorded over a larger range of epicentral distances (∼0 to >600 km); in Chile, where most earthquakes were offshore but the seismometers were on land, aftershocks had minimum source-station distances up to 200 km.

Again, we collated the available data into our own waveform server. We selected from up to 290 three-component broad-band stations for events between November 2011 and October 2014 (and an additional 284 stations when the TA stations were in the study region). While this test case has a much larger data selection than the Maule case study, many of the stations within independent networks (e.g. the Cooperative New Madrid network) occur in clusters that plot within very localized regions on the focal sphere, thus providing redundant data. For most events, traces from tens of stations were used for the RMT inversions.

3 SYNTHETIC SEISMOGRAMS FOR HYPOTHETICAL FOCAL MECHANISMS AND NETWORKS

The distribution of seismometers about an earthquake's hypocentre affects the ability of a moment tensor inversion to constrain the best-fitting focal mechanism (Šílený *et al.* 1996; Ford *et al.* 2009; Pesicek *et al.* 2012). The ideal seismic network covers a large range of azimuths and distances from the earthquake; this facilitates widespread coverage of the focal sphere. However, in most source zones, achieving ideal network geometry is difficult. For example, for most earthquakes recorded by the IMAD network, stations covered less than half the focal sphere azimuthally over a limited range of distance, primarily because of narrow east–west network aperture and events occurring mostly offshore in the seismogenic zone of the Nazca subduction thrust.

Here, we observe how certain characteristics of network geometry affect the sensitivity of inverted moment tensors to the nodal planes' strike and dip. We produced synthetic seismograms using Generic Seismic Application Computing (GSAC, Herrmann *et al.* 2004) for numerous network geometries, which include different numbers of stations and varying station positions (see below for details), and two consistent focal mechanisms: (1) a M_W 4.0 earthquake occurring at 20 km depth with a strike, dip and rake of $0°$, $45°$ and $90°$ (i.e. a pure dip-slip event) and (2) M_W 4.0 earthquake

occurring at 5 km depth with a strike, dip and rake of 315°, 90° and 0° (i.e. a pure strike-slip event). We tested how the following four network geometry characteristics affected RMT sensitivity:

(1) *Event-station distance*: Four stations at azimuths of 0°, 90°, 180° and 270° are placed at an equal distance from the epicentre. Six tests are conducted, with distance set to 25, 50, 100, 200, 400 and 600 km, respectively.

(2) *Azimuthal coverage*: Four stations are placed at 200 km from the epicentre and distributed evenly over limited azimuthal ranges, with the first station placed at 0°. Tests are conducted for five azimuthal ranges: 45°, 90°, 120°, 180° and 270°. In practice, coverage of 270° is identical to full coverage, since the stations are separated by 90° and a station is placed at due north (0° or 360°).

(3) *Event-station azimuth*: The four stations in (1) at a distance of 200 km (chosen for realistic proximity of earthquakes of the Maule and Oklahoma sequences to their respective stations) are repositioned with respect to the strike of the focal mechanism. The entire system is rotated 30°, 45° and 60° clockwise from the orientation in (1).

(4) *Network density:* Stations are placed at 200 km from the epicentre and distributed evenly azimuthally. Tests are conducted for five hypothetical networks: with 3, 4, 12, 24 and 36 stations.

For each network-source pairing, we computed the double-couple component of an RMT solution using a grid search method that maximizes the objective function—the data-model fit between observed (synthetic) and predicted time-series velocity waveforms—according to the method of Herrmann *et al.* (2011b, discussed in Appendix A). We then observed how the RMT data-model fit changed when strike and dip were individually varied within a 35° parameter space in either direction of the best-fitting solution. We compared the range of acceptable strikes and dips among the tests, defining 'acceptable' as any solution with a fit value greater than 90 per cent of the best-fitting solution (100 per cent, or equal to 1.0, for these tests, since the inversions used synthetic data without noise). The inversion process, test network geometries, and analysis strategy are discussed in detail in Appendix B.

3.1 Results

The results in this section demonstrate (1) how simple geometric qualities of a seismic network affect the moment tensor sensitivity and (2) how faulting type (dip-slip versus strike-slip) interplays with network geometry to complicate our analysis of moment tensor sensitivity. Refer to Appendix B for a detailed analysis and figures that support the generalized results.

For the reverse mechanism, strike constraint varies only slightly with event-station distance (Fig. A1a). The range of acceptable fits improves (decreases) when stations align azimuthally parallel and perpendicular to the nodal planes (Figs A2a and A3a), and when fewer stations (as few as four) are used in the inversion (Fig. A4a). Among the four tests (varied event-station distance, azimuthal coverage, event-station azimuth and network density), strike constraint ranges from 30° to >50°. The upper limit of this range is unknown, because for strike variations rotated in one direction from the best-fitting strike, all tested values within the parameter space yield acceptable fits. Dip constraint for the reverse mechanism improves for station geometries with smaller source-station distances (Fig. A1b), with more complete azimuthal coverage (Fig. A2b), with stations positioned azimuthally parallel and perpendicular to the nodal plane (Fig. A3b), and with fewer stations (as few as four)

used in the inversion (Fig. A4b). Among tests, dip constraint ranges from 12° to 33°. In most cases, dip is better constrained than strike for this reverse mechanism.

For the strike-slip mechanism, strike constraint varies only slightly with event-station distance for pairings beyond 25 km (Fig. A1c). On the other hand, dip constraint improves significantly for intermediate source-station distances (of the tested distances, 50–400 km, Fig. A1d). Both strike and dip constraints improve with complete azimuthal coverage (Figs A2c and d), with stations located centrally between nodal planes (Figs A3c and d), and with fewer stations (as few as four) used in the inversion (Figs A4c and d). Among tests, strike constraint ranges from 7° to >45° and dip constraint ranges from 29° to >60°. In most cases, strike is better constrained than dip for this strike-slip mechanism.

Based on the tests performed here, both faulting style and station geometry affect RMT sensitivity. Some characteristics of station geometry impact RMT sensitivity in comparable ways for both focal mechanisms. For example, varying the azimuthal coverage and rotating the network about the nodal planes introduces asymmetry to the strike fit-falloff curves for both of the tested focal mechanisms; dip remains more or less symmetric in both cases. On the other hand, the reverse mechanism is better-constrained by stations positioned near the nodal planes, while the strike-slip mechanism is better constrained when stations plot centrally between the nodal planes. In both cases, stations are at azimuths where radiation patterns for their respective mechanisms change rapidly. Additionally, dip is usually better constrained than strike for the dip-slip mechanism, while strike is better constrained for the strike-slip mechanism. Again, this is based on azimuthally variable radiation patterns, which change rapidly with fault dip for dip-slip mechanisms, but more quickly with strike for strike-slip mechanisms.

4 REAL AND SYNTHETIC SEISMOGRAMS FOR OBSERVED FOCAL MECHANISMS AND STATION DISTRIBUTIONS

Here, we examine the strike and dip fit falloff for source-station pairings that have occurred during true seismic deployments. We evaluate the effects of station distribution and faulting type on strike and dip fit falloff for three scenarios, and for two previous or existing seismic deployment test cases: (1) the International Maule Aftershock Deployment (IMAD) following the 2010 M_W 8.8 Maule earthquake and (2) the group of temporary and permanent stations monitoring the ongoing sequences of earthquakes in Oklahoma and southern Kansas. These data are described in Section 2.

In Scenario 1, we compute the double-couple components of RMTs for each earthquake in our two test cases, as well as relative fits for the solution space surrounding the best-fitting model, for fixed hypocentral coordinates according to relocations determined in Hayes *et al.* (2013). In Scenario 2, we generate synthetic waveforms with noise for the computed focal mechanisms and source–station pairings from Scenario 1, and use these synthetic data as input to the RMT inversion. We compare the observed fit falloffs for these synthetic scenarios with those from the real data inversions in Scenario 1. In Scenario 3, we repeat the synthetic inversions in Scenario 2, expanding the input data to include all stations deployed at any point over the monitoring period of each network. This scenario tests how well the entire network (or set of networks) can constrain RMTs, as opposed to just those stations that were online and recording high-quality data for a given earthquake.

Table 1. Western United States velocity model used in all RMT computations. From left to right, the columns are depth (H), P-wave velocity (V_P), S-wave velocity (V_S), density (Rho), P-wave attenuation (Q_p) and S-wave attenuation (Q_s).

H (km)	Vp (km s^{-1})	Vs (km s^{-1})	Rho (gm cc^{-1})	Q_p	Q_s
1.9000	3.4065	2.0089	2.2150	3.02E-03	6.79E-03
6.1000	5.5445	3.2953	2.6089	3.49E-03	7.84E-03
13.0000	6.2708	3.7396	2.7812	2.12E-03	4.76E-03
19.0000	6.4075	3.7680	2.8223	1.11E-03	2.49E-03
30.0000	7.9000	4.6200	3.2760	1.64E-11	3.70E-11
0.0000	7.9000	4.6200	3.2760	1.64E-11	3.70E-11

Only those Scenario 1 RMTs deemed 'repeatable' were used for sensitivity analysis and in Scenarios 2 and 3. RMTs from real-data are included in further analysis if they meet two criteria: (1) they yield absolute goodness-of-fit values—computed in a least-squares sense—greater than 0.5, and (2) the computed strike, dip and rake values could be reproduced to within 10° by two data selections and inversions performed independently of each other by two different scientists, deeming them 'repeatable RMTs'.

The Maule aftershock RMTs used here were compiled in Hayes *et al*. (2013); those for the Oklahoma and Kansas events were computed for the second time in this study and compared to McNamara *et al*. (2015a). In Scenarios 2 and 3, we produce the synthetic data using GSAC as in our preliminary tests, but add random noise to the synthetic data (based on an average of the USGS Albuquerque New High and Low Noise Models, NHNM and NLNM, a range of −165 to −120 dB; Peterson 1993). We use the inversion configurations (cut times and frequency ranges, described in Appendix A) from Scenario 1 on an event-by-event basis. For all RMTs in all scenarios, we use the 1-D western United States (WUS) velocity model in Table 1, consistent with the initial RMTs by Hayes *et al*. (2013) and McNamara *et al*. (2015a). While these previous studies determined that the WUS model accurately reflects the regional waveform dispersion, the RMT inversions performed here are also sensitive to the velocity model parameters. This frequency-dependent sensitivity is beyond the scope of our study.

4.1 Test case: the M_w 8.8 Maule earthquake aftershock sequence

Hayes *et al*. (2013) used RMTs for the ∼500 highest magnitude aftershocks of the 2010 M_W 8.8 Maule earthquake to constrain the seismotectonic framework of the coseismically ruptured region of the subduction zone. In evaluating the uncertainty and sensitivity of the RMTs for those 293 aftershocks (M_W 3.67–6.33) with repeatable focal mechanisms (Fig. 1), they found that a surprisingly large range of strikes (∼50°) and dips (∼40°) yield fits within 10 per cent of the best-fitting solution (Fig. 2). They attributed the low sensitivity to changes in strike and dip to the large gap in azimuthal coverage intrinsic to the IMAD seismic network.

Here, we use the RMTs from Hayes *et al*. (2013) to evaluate the ability of the IMAD deployment to constrain strike and dip. We compare the Scenario 1 results to the 'best possible' ranges of acceptable strike and dip determined for synthetic seismograms in Scenarios 2 and 3.

A detailed analysis of RMT magnitude sensitivity has not been conducted as part of this study. However, we note that we do not constrain moment at any stage of the grid search process. In the most extreme case—Scenario 1 (real data)—the magnitude for Maule aftershock RMTs varies by up to M_W 0.32 among the acceptable solutions. Previous work (e.g. Kanamori & Rivera 2008) has demon-

strated that seismic moment trades off with dip for shallowly dipping focal mechanisms, dip increasing as moment decreases. This persists within the parameter spaces of individual events; however, we do not see an overlying trend between magnitude range and any best-fitting fault parameter. Because we fixed depth in the inversions, magnitude variations depend on changes in the inverted fault parameters, and thus the source radiation pattern rather than simply trading off with source-station distance.

Scenarios 1 and 2: Comparison between real versus synthetic data for observed focal mechanisms and existing station distributions

This pair of scenarios evaluates the sensitivity of the 293 Maule aftershock RMTs from Hayes *et al*. (2013) to small changes in strike and dip; these RMTs mostly represent a near-pure dip-slip earthquake with large gaps in azimuthal coverage. To do so, we compare the ranges of acceptable strike and dip determined for RMTs computed for observed earthquakes from recorded data (Scenario 1; herein termed 'real earthquakes') to those for synthetic data that represents the observed earthquakes (Scenario 2). For consistency between the Scenarios, Scenario 2 includes only stations used to compute the real RMT for each earthquake in Scenario 1. Thus, the results indicate how well constrained our RMTs could be under the influence of only well-behaved noise (−165 to −120 dB, see above) and not other factors that contribute to observed seismograms (e.g. site effects at a station, anisotropy, etc.); however, they do not directly portray the limitations of a seismic network with IMAD geometry, because in most cases not all stations were used in the real-data inversions.

Fig. 2 and Hayes *et al*. (2013) show the ranges of acceptable strikes and dips for each of the 293 RMTs computed for Maule aftershocks, divided based on fit value. Here, we analyse how the range distribution among events varies spatially. Figs 3 and 4 include contour plots for the RMTs from real data (Figs 3a and 4a), those from synthetic data with noise (Figs 3b and 4b), and the difference between the two (real minus synthetic, Figs 3c and 4c) for strike and dip, respectively.

Ranges of acceptable strike for the real data (Fig. 3a) span from 9° to >71°, averaging 56°. Generally, the ranges decrease as azimuthal coverage improves, and also when stations are at distances <50 and >50 km. Spatially, this corresponds to improved constraint from west–northwest to east (perpendicular to the coast), since the stations close to or onshore have inherently wider coverage by the coastal IMAD stations, and are closer in distance to the nearest stations. We also observe less variability in strike and dip for the northernmost aftershocks than those in the south. The network extends beyond the included aftershocks in the north, but not in the south, and thus the northern extent has more complete azimuthal coverage. Additionally, the coastline trends east of north along the whole aftershock region, parallel to the strike of both nodal planes
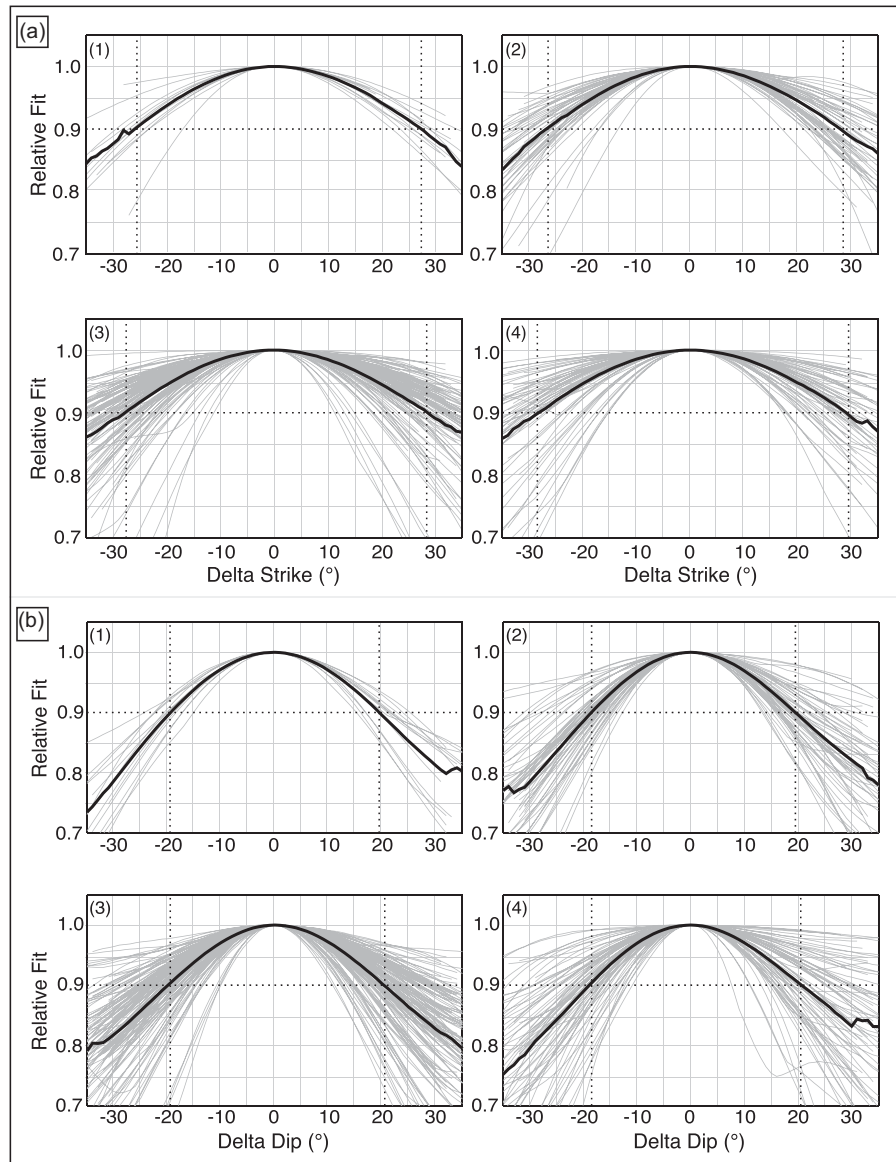
Figure 2. Adapted from Hayes *et al*. (2013). 294 Maule aftershocks with repeatable RMT solutions divided into four quality groups based on absolute fit: (1) greater than 0.8, (2) 0.7–0.8, (3) 0.6–0.7 and (4) 0.5–0.6. (a) Relative strike and (b) dip are plotted in grey for all events in each group. The thick, solid black lines show the average strike or dip falloff for the respective group. Horizontal dotted black lines show the cut-off for acceptable solutions at 0.9 relative fit. Vertical dotted black lines coincide with the intersection of the acceptable solution and average falloff lines, bounding the average values of delta strike and delta dip (with respect to the best fit of each parameter) that have a relative fit within 90 per cent of the best-fitting solution. Range of acceptable fits is not directly correlated with the best-fitting value, indicating that uncertainty range is characteristic of the data set, not varying quality of the inversions by Hayes *et al*. (2013).

for most RMTs, further increasing the azimuthal gap for the southernmost aftershocks to include the azimuths of both nodal planes. We compared the magnitudes of aftershocks in this northern region (the Pichilemu cluster; Hayes *et al.* 2013, and references therein) to the full data set, finding mean and median magnitudes of M_W 4.4 and M_W 4.3 for both; thus, the lesser variability in the northern region is independent of magnitude. The Scenario 2 results, computed for synthetic data with noise (Fig. 3b), yield much smaller ranges of acceptable strike than the real data, spanning 20° to 62° with an average range of 46°; however, the trends observed in this plot generally agree with those for the real data.

Fig. 3(c) compares strike constraint for RMTs computed using real versus synthetic data with noise. The difference in ranges of

acceptable fit spans −10° to 50°; positive values correspond to RMTs that were better constrained by the synthetic data. The trends observed for the independent Scenarios (Figs 3a and b)— better constraint with improved azimuthal coverage—persist in this difference plot. Ranges of acceptable strike match most closely between Scenarios 1 and 2 for onshore earthquakes, and diverge to the west; this suggests that data quality, in addition to station geometry, impacts strike sensitivity. We applied uniform noise to the entire synthetic data set used in Scenario 2, but in reality, events farther offshore may produce noisier waveforms or be subjected to stronger scattering effects. The waveforms must travel much farther before reaching seismometers, and also likely travel through a more complicated velocity structure, which
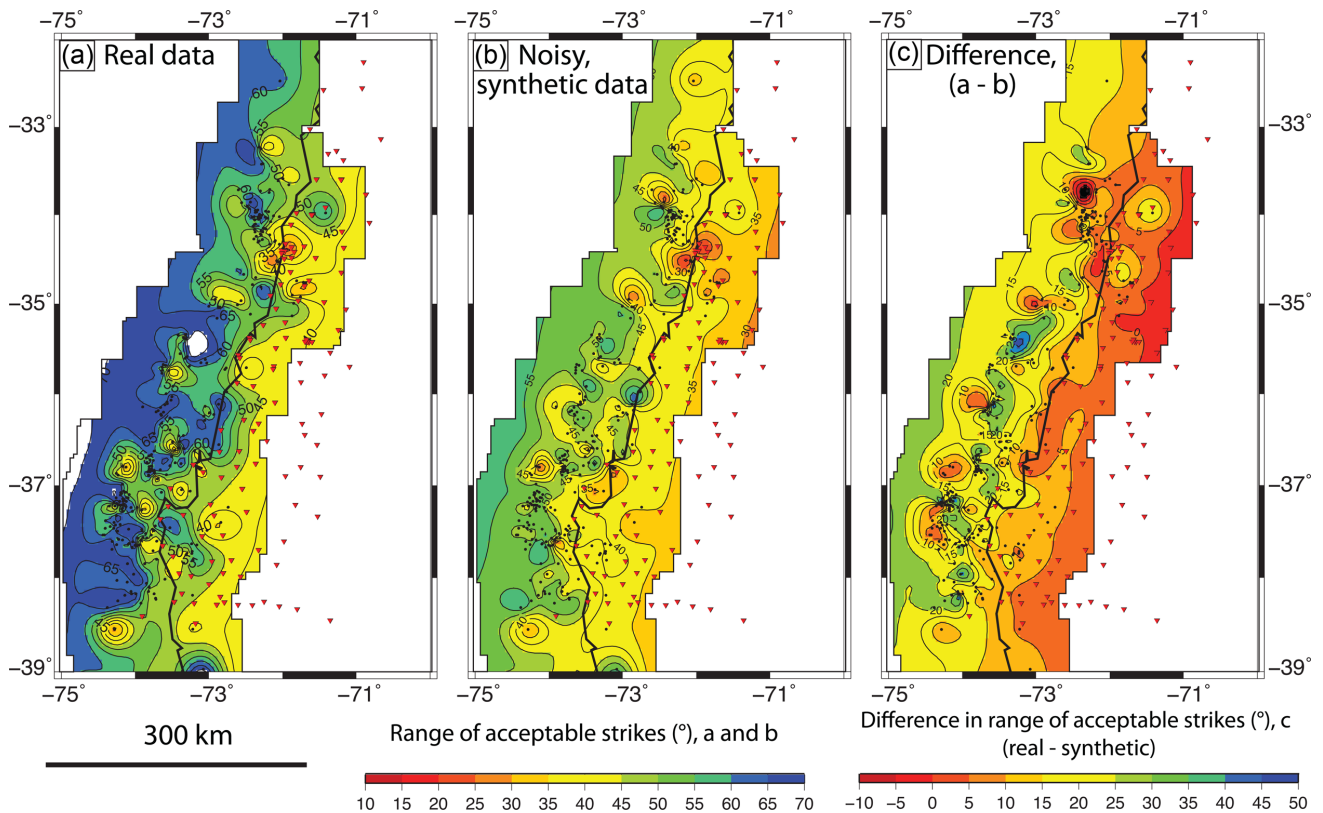
Figure 3. Spatial distribution of range of acceptable strikes for 293 aftershocks of the 2010 Maule earthquake, Scenarios 1 and 2. Black dots are earthquake epicentres. Inverted red triangles are IMAD station locations. The thick black line is the coastline of Chile. (a) Scenario 1: range of acceptable strikes for RMTs using real data. (b) Scenario 2: range of acceptable strikes for RMTs using synthetic data with noise. (c) Scenario 1 minus Scenario 2: difference in range of acceptable strikes when real versus noisy synthetic data are used. Contour interval for all plots is 5°.

includes both the subducting Nazca and overriding South American plates.

Ranges of acceptable dip for the real data (Fig. 4a) generally follow the same trends as strike, but have lesser variability, spanning 18° to 71° with a mean of 44°. Dip is best constrained for onshore epicentres due to source-station variability and good azimuthal coverage. The southernmost RMTs are most poorly constrained, but to a lesser degree than for strike. This suggests that dip constraint gains more from stations distributed throughout the focal sphere than from stations positioned near the nodal planes. As for strike, the Scenario 2 synthetic data (Fig. 4b) yields smaller ranges of acceptable dip than the real data (20° to 60° with a mean of 31°), with mostly persistent trends but one exception: the farthest offshore RMTs for the synthetic data do not show increasingly larger ranges. This is supportive of results from Section 2 and Appendix B, which show that increasing azimuthal gap only affects the range of acceptable dips slightly. An alternative explanation is that waveforms from earthquakes farther offshore are subjected to higher degrees of noise, as we suggested in our analysis of strike sensitivity, and so we see increasing ranges of acceptable fit in the real data, but not in the synthetic wave with constant added noise.

Fig. 4(c) compares dip constraint for RMTs computed using real versus synthetic data with noise. The difference in ranges of acceptable fit spans −10° to 40°. Most of the difference values are positive, indicating better constraint by the synthetic data. Additionally, the spatial trend of increasing value farther offshore, which in the real data corresponds to poorer constraint on dip, persists in this difference plot. As for strike, both these observations likely result from the uniform way in which we incorporated noise into the syn-

thetic waveforms. A few outliers far offshore with low or negative differences, which are also outliers in the real data and have lower ranges than nearby RMTs, suggest that waveforms for the most important stations for those earthquakes—those that change rapidly with small changes in dip—had higher signal-to-noise ratios than we incorporated into our synthetic tests. Alternatively, the outlier events may have occurred in different structural units of the forearc, and thus have contrasting velocity structures that are not completely accounted for in the inversion.

In summary, strike constraint for dip-slip earthquakes—as observed in the Maule aftershock sequence—improves with source-station distance variability and azimuthal coverage, particularly when stations are azimuthally located near the modelled *P*-wave radiation pattern nodal planes. Dip is generally better constrained under this network geometry, depending less on azimuthal coverage, and gaining more from a wide station distribution than stations aligned azimuthally near the nodal planes.

Scenario 3: Synthetic data for observed earthquakes and all available stations

When synthetic data with noise for all network stations are used, the range of acceptable strike spans 20–65°, 5° larger than when only the stations used in the real RMT inversion are included. However, the mean value drops to 45° (versus 46°). Because the mean decreases despite the range expanding, we can suggest that in general, use of more stations can improve the strike constraint on the RMT, but in some cases makes the RMT less sensitive to small changes in strike.
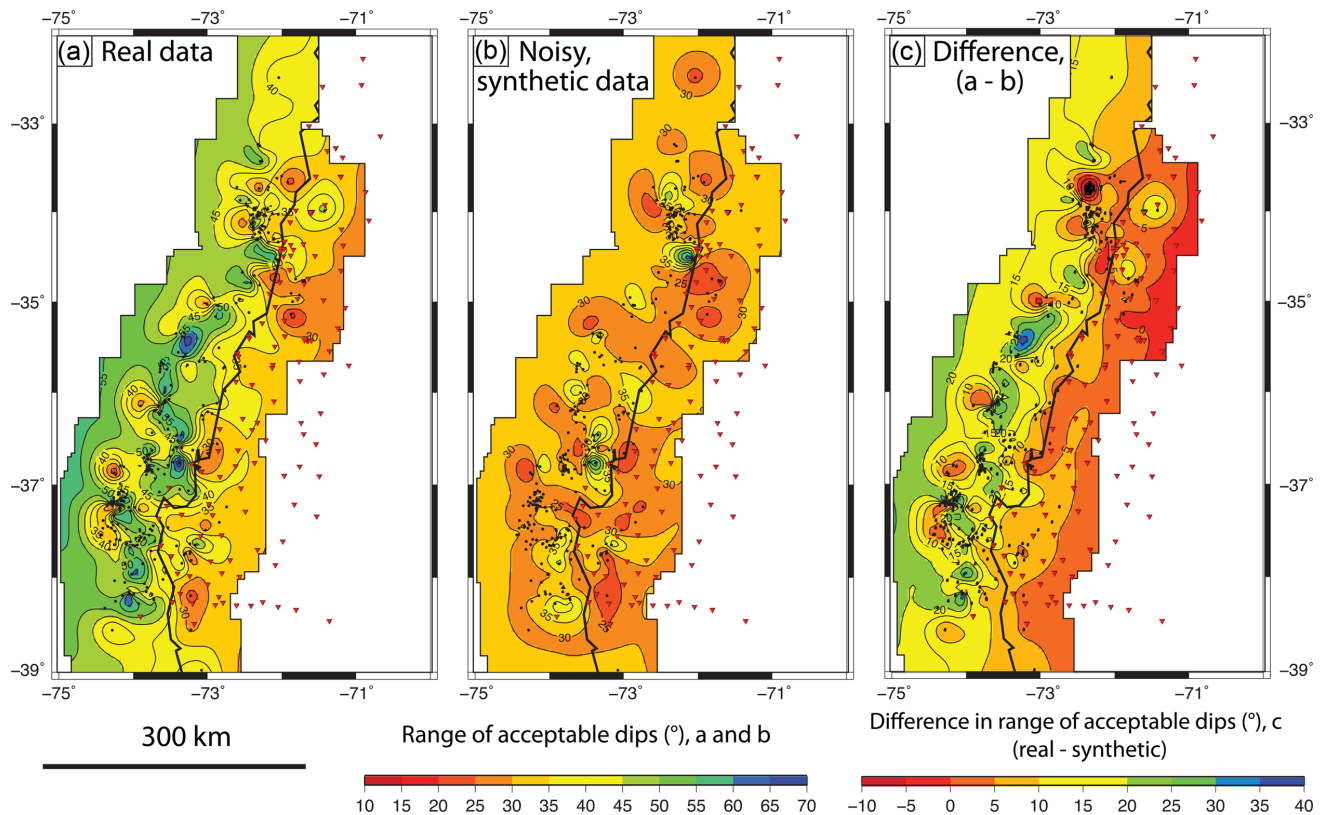
Figure 4. Spatial distribution of range of acceptable dips for 293 aftershocks of the 2010 Maule earthquake, Scenarios 1 and 2. Black dots are earthquake epicentres. Inverted red triangles are IMAD station locations. The thick black line is the coastline of Chile. (a) Scenario 1: range of acceptable dips for RMTs using real data. (b) Scenario 2: range of acceptable dips for RMTs using synthetic data with noise. (c) Scenario 1 minus Scenario 2: difference in range of acceptable dips when real versus noisy synthetic data are used. Contour interval for all plots is 5°.

This result is similar to the density tests in Section 2; by including more stations, the RMT inversion puts less weight on each, lessening sensitivity to small changes in individual waveforms.

The spatial trends we see for strike in Scenario 3 (Fig. 5a) are consistent with Scenarios 1 and 2 (Figs 3a and b). A west–northwestward increase in range of acceptable strikes places many of the best-constrained RMTs near or onshore, and many of the most poorly constrained RMTs far offshore and at the southern-most extent of the network. Thus, the spatial trends observed in Figs 3(a) and (b) do not depend on the station subsets used for individual inversions, but represent the network as a whole. Fig. 5(b) shows the difference between Scenarios 2 and 3. The region has a near-uniform difference value of 0° ± 2°, except a few outliers better represented when all stations were included.

The ranges of acceptable dips in Scenario 3 span 19° to 61° with a mean of 31°, though less than 10 per cent of the RMTs have ranges larger than 40°. These limits are almost identical to those from Scenario 2, and the mean value does not change. Spatially, however, the scenarios differ; when the entire IMAD network is used (Fig. 6a), the data set is uniform at ∼30° (very close to the mean value), with a few scattered outliers. Fig. 6(b) shows how the difference between Scenarios 2 and 3 varies spatially; the Appendix E compares the pure range values for each event. The data sets mostly differ by <1°; however, the few significant outliers correspond to the RMT outliers in Fig. 6(a), indicating that for those events, the station subset did impact RMT sensitivity to changes in dip. The network may have poorly resolved these earthquakes, or alternatively, the earthquakes may have occurred late in the aftershock sequence when many stations had already been decommis-

sioned, or early in the sequence before many of the stations were installed.

4.2 Test case: regional seismicity in Oklahoma and southern Kansas

In this study, we analyse the subset of these earthquakes for which we could compute a repeatable RMT (Fig. 7). This amounts to 49 earthquakes (48 events M_W 3.17–4.83 and one event M_W 5.59) between November 2011 and October 2014. Fig. 8 shows the strike and dip fit falloff for these 49 RMTs.

The several permanent and temporary seismic stations (Fig. 7, McNamara *et al.* 2015a) allowed detection and RMT computation for these earthquakes. Due to a sudden increase in seismicity rate in Oklahoma, several new seismic stations were deployed in 2012, which complemented the existing networks to provide more complete azimuthal coverage and variable source-station distances (∼0 to >600 km). This network geometry strongly contrasts the station coverage in Chile, where offshore earthquakes and narrow network aperture limited azimuthal coverage of most aftershocks to ∼50 per cent with minimum source-station distances up to 200 km.

Here, we use the RMTs from McNamara *et al.* (2015a) to evaluate the ability of the regional network to constrain strike and dip. We compare the Scenario 1 results to the 'best possible' ranges of acceptable strike and dip determined for synthetic seismograms in Scenarios 2 and 3.

As with the Maule test case, we do not include a detailed analysis of RMT magnitude sensitivity despite letting magnitude vary within
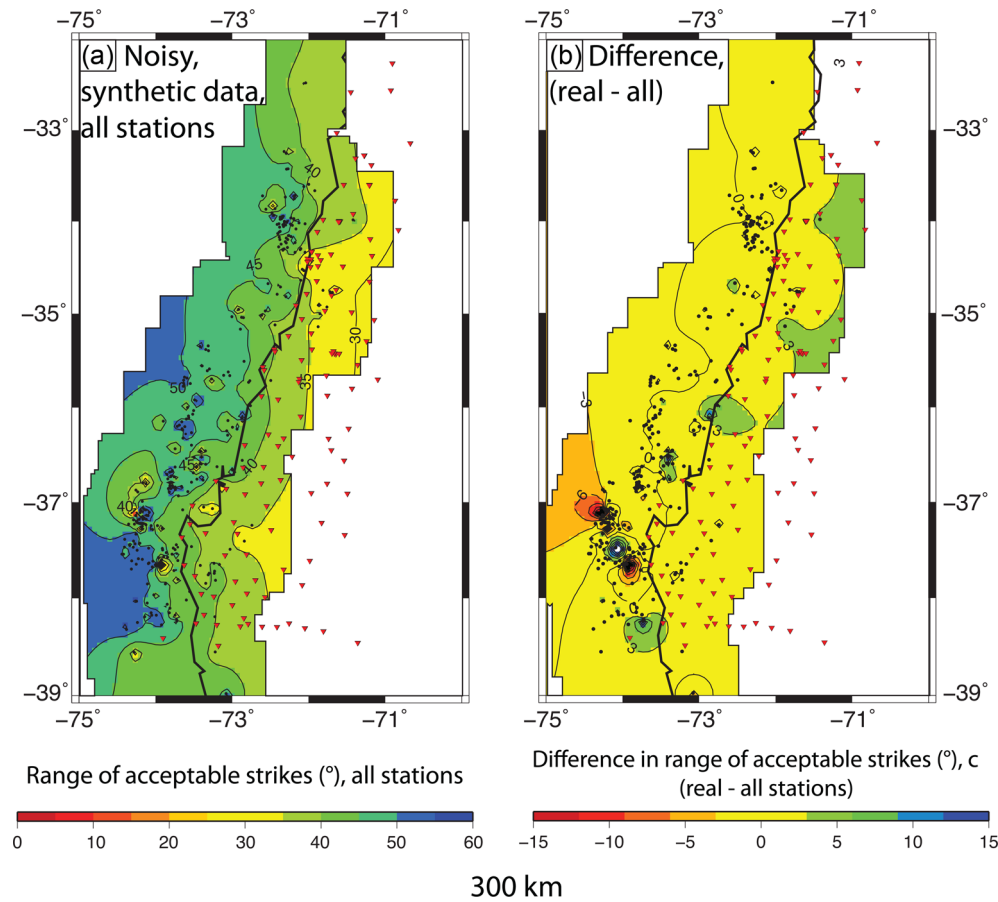
Figure 5. Spatial distribution of range of acceptable strikes for 293 aftershocks of the 2010 Maule earthquake, Scenario 3. Black dots are earthquake epicentres. Inverted red triangles are IMAD station locations. The thick black line is the coastline of Chile. (a) Scenario 3: ranges of acceptable strike when synthetic data for all stations in the IMAD deployment are used. Contour interval is 5°. (b) Scenario 3 minus Scenario 2: difference in range of acceptable strikes when synthetic data with noise for all stations versus those from the real inversion are used. Contour interval is 1°.

the grid search. In the most extreme case—a Scenario 3 RMT (synthetic data, all stations)—magnitude varies by M_W 0.28 among the acceptable solutions. Again, this magnitude variation does not seem to depend on any fault parameters.

Scenarios 1 and 2: Comparison between real versus synthetic data for observed focal mechanisms and true station distributions

This pair of scenarios evaluates the sensitivity of the 49 Oklahoma and Kansas earthquake RMTs to small changes in strike and dip. As with the Chilean events, we evaluate the ranges of acceptable strike and dip for real earthquakes (Scenario 1), and compare them to ranges from synthetic data for observed earthquakes at real source-station pairs (Scenario 2). Most RMTs included in this test case represent northwest–southeast striking, vertically dipping left-lateral strike-slip focal mechanisms, comparable in faulting style and orientation to the hypothetical strike-slip earthquake in Section 2; therefore, we also compare the patterns observed here to those from the purely synthetic inversions.

Fig. 9(a) shows the spatial variation in range of acceptable strikes for Oklahoma RMTs computed using real data, values spanning 14–44° with a mean value of 26°. The better constraint on strike than in Chile likely results from the more azimuthally complete station geometry, especially near the nodal planes, as we observe in the Section 2 synthetic tests, and more variable source-station

distances. The Scenario 2 ranges of acceptable strike computed from synthetic waveforms with noise (Fig. 9b) compare closely to the Scenario 1 ranges, spanning 17–44° with a mean value of 25°. This suggests that we were able to constrain strike on the real RMTs about as well as we could have under conditions of only well-behaved noise (note that—as in Test Case 1—these synthetic seismograms do not account for site effects, anisotropy, etc.). The difference plot in Fig. 9(c) is dominated by near-zero values (−1° to 1°), further exemplifying this accomplishment. Appendix C discusses two outliers in Figs 9(a) and (c).

Fig. 10(a) shows the range of acceptable dips for the Oklahoma RMTs computed using real data. The ranges span from 38° to >71° with a mean range of 60° and only six focal mechanisms with ranges <50°, with overall ranges much larger than those computed for the Maule aftershocks. These ranges initially seem quite large, spanning more than half the possible dips of 0°–90°. However, the searched parameter space centres around the best-fitting RMT, which most often occurs on steeply dipping planes (near-90°). Thus, the dip-space ranges from ∼55° to ∼125° (e.g. many of the acceptable solutions allow the fault to dip supervertically, or subvertically with the fault strike rotated by 180° but with the fault blocks still moving in the same direction with respect to one another). The range contours in Fig. 10(a) mostly trend west–northwest to east–southeast and increase in value towards the northeast. These trends and range values contrast our initial hypothesis that azimuthal coverage should
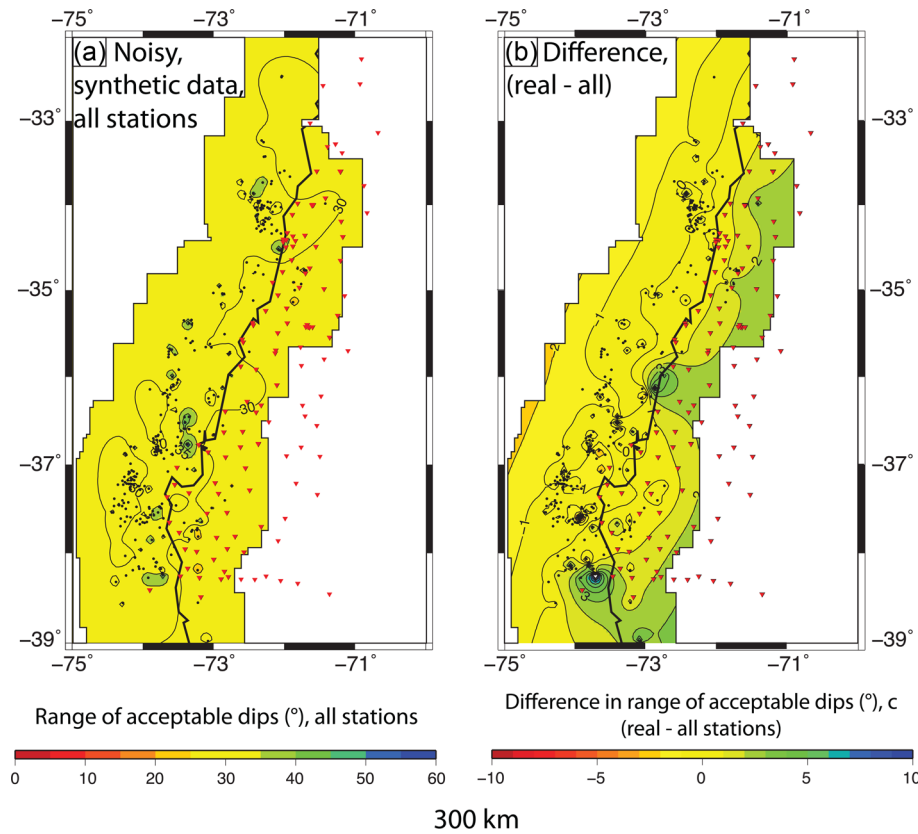
Figure 6. Spatial distribution of range of acceptable dips for 293 aftershocks of the 2010 Maule earthquake, Scenario 3. Black dots are earthquake epicentres. Inverted red triangles are IMAD station locations. The thick black line is the coastline of Chile. (a) Scenario 3: ranges of acceptable dip when synthetic data for all stations in the IMAD deployment are used. Contour interval is 5°. (b) Scenario 3 minus Scenario 2: difference in range of acceptable dips when synthetic data with noise for all stations versus those from the real inversion are used. Contour interval is 1°.

improve RMT constraint (recall that station coverage generally increases from west to east; see Fig. 7), but are supported by our observations of the synthetic and purely hypothetical tests in Section 2. The Scenario 2 ranges of acceptable dip computed using the synthetic waveforms with noise (Fig. 10b) span 22° to >71°, with a mean value decreased by 8–52°, suggesting that for most RMTs, we assigned a lower signal-to-noise ratio than that which existed in the real data. This result contrasts our comparable Scenarios 1 and 2 ranges of acceptable strike, perhaps implying varying levels of noise among station components, an issue we address more carefully below.

The general pattern in the synthetic data ranges of acceptable dip (Fig. 10b) compares to that in the real data: the RMTs with the largest ranges are in the southeast, among good station density and azimuthal coverage, while those with the smallest ranges are in the northwest with less complete azimuthal coverage. Most of the outliers in Figs 10(a) and (b) with anomalously low ranges of acceptable dip correspond to dip-slip events. These results suggest that in addition to station distribution, style of faulting may impact dip sensitivity as suggested by Robinson & Cheung (2010), an issue discussed below.

Fig. 10(c) shows the difference between ranges computed for the real and synthetic RMTs. The contours appear dominated by outliers, a contrast that—as suggested in previous analyses—likely depends on our uniform addition of noise to the synthetic data compared to the real data quality.

We illustrate faulting style impact on range of acceptable dip by separating RMTs into two groups of faulting events, divided based on rake. Forty-one predominantly strike-slip RMTs with <20° dip-slip components have ranges of acceptable dip spanning 38° to >71° and a mean value of 64° (Fig. 11a), while eight dip-slip RMTs with >20° dip-slip components span 38° to 70° with a mean value of 50° (Fig. 11b, though only one has a range larger than 56°; when excluded the mean drops to 47°). Qualitatively, the difference in ranges is easy to see in Fig. 11; the contours show increasing range from southwest to northeast; however, the contours in Fig. 11(b) are shifted northeastward compared to those in Fig. 11(a), indicating lower ranges of acceptable dip for RMTs with a dip-slip component. Again, this cautions us to consider faulting style when analysing trends in the range of acceptable dips (Stich *et al.* 2003; Robinson & Cheung 2010), rather than station distribution alone.

In summary, well-distributed seismic stations—both azimuthally and in source-station distance—improve constraint on RMT strike for strike-slip earthquakes as seen in the ongoing Oklahoma and southern Kansas earthquake sequence. Dip constraint, however, does not necessarily improve with improved station distribution; pure strike-slip earthquake RMTs are insensitive to small changes in dip, while a dip-slip component as small as 20° greatly improves dip constraint.

Scenario 3: Synthetic data for observed earthquakes and all available stations

Scenario 3 tests the potential of the permanent and temporary deployments monitoring the ongoing earthquake sequence in southern
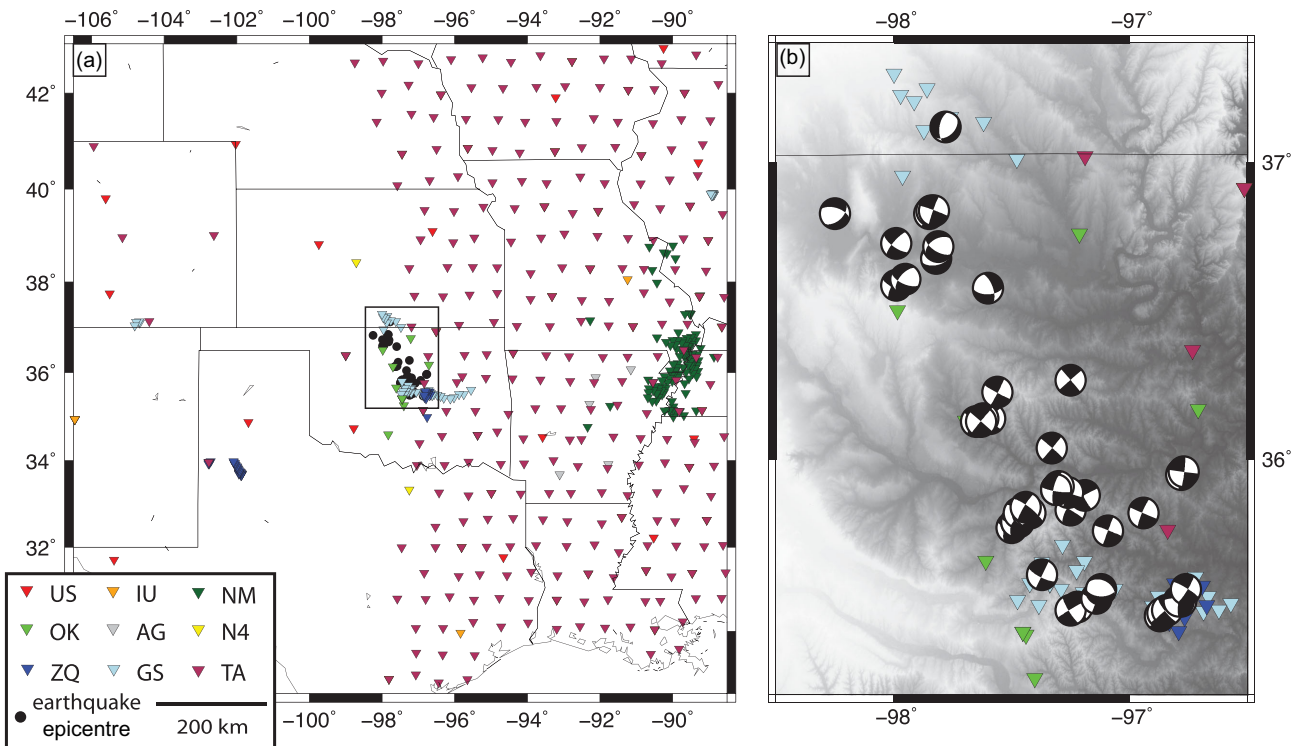
Figure 7. Seismic networks that detected the Oklahoma and Kansas earthquakes used in this study and earthquakes used in the Oklahoma and southern Kansas test case. (a) All stations within 600 km of an epicentre; candidate stations for an RMT inversion. Filled black dots are earthquake epicentral locations. Inverted triangles show seismometer locations, coloured by seismic network. US, United States National Seismic Network; IU, IRIS/USGS Global Seismograph Network; NM, Cooperative New Madrid Seismic Network; GS, USGS NEIC 1990; OK, Oklahoma Seismic Network; AG, Arkansas Seismic Network; N4, Central and Eastern US Network (UC San Diego 2013); ZQ, Oklahoma RAMP Network (Keranen 2011). (b) Focal mechanisms and study area for this test case; zoom in on black rectangle in (a). Station colours correspond to networks listed in (a). Most earthquakes are nearly pure strike-slip, but a few have noticeable normal components.

Kansas and Oklahoma, as opposed to just those stations that were useful on an event-by-event basis. We apply the synthetic aspect of Scenario 1, but adjust our approach to better address the full resolving potential of the network by using all stations that were located within 600 km of an earthquake epicentre at any time during their deployment *except* those that compose the Transportable Array (TA). The TA stations occupied a north–south swath that included the eastern half of Oklahoma during the beginning of our study period, and represents a station distribution that cannot necessarily by expected from a permanent or rapid deployment. An additional scenario (Scenario S1) repeats Scenario 3 but includes TA stations; Scenario S1 is discussed and compared to Scenario 3 in Appendix D.

Fig. 12(a) shows the spatial variation among the ranges of acceptable strike for Scenario 3. The ranges span 15–54° with a mean value of 28°, a value only 3° larger than in Scenario 2 (though only one earthquake has a range larger than 43°, and when excluded the mean drops by 0.5°). Fig. 12(b) plots the spatial difference between Scenarios 2 and 3; Appendix E compares the ranges computed for each against each other. For many events, strike constraint improved with more stations, while for others uncertainty increased. A lacking spatial trend suggests that ranges may depend more on the number and placement of stations used in the real inversion, event timing, magnitude, depth and faulting style than epicentral location.

Fig. 13(a) shows the spatial variation among ranges of acceptable dip for Scenario 3. The ranges span 17–70° with a mean of 46°, a value 6° lower than that in Scenario 2. Fig. 13(b) plots the difference between Scenario 2 and Scenario 3; Appendix E compares the ranges computed for each against each other. The difference in range of acceptable dip generally increases from west to east. For many RMTs, dip is better constrained when computed with only the stations used in the real inversion; this characteristic resembles the synthetic density tests (Appendix B), which show that denser station coverage does not necessarily provide better constrained dip for strike-slip earthquakes.

We were intrigued by the poor constraint on dip for this set of shallow, strike-slip earthquakes, despite an azimuthally complete station distribution with variable source–station distances. Thus, we further evaluated this result by examining the waveforms themselves, and observing how their shapes and magnitudes changed as the RMT dip was changed in small increments.

4.3 Evaluation of individual station components with changing dip

To better understand why RMT fit is insensitive to changes in dip for strike-slip earthquakes in Oklahoma, we visually inspected the waveforms for each component of each station that plots near the focal planes and observed how they change with incremental adjustments to dip in our Green's functions.

While the radial and vertical components undergo some degree of change in shape and amplitude, the transverse component waveforms for different dips are virtually indistinguishable (Fig. 14). In order to better evaluate how much the transverse components contribute to the large range of acceptable dips for this source depth
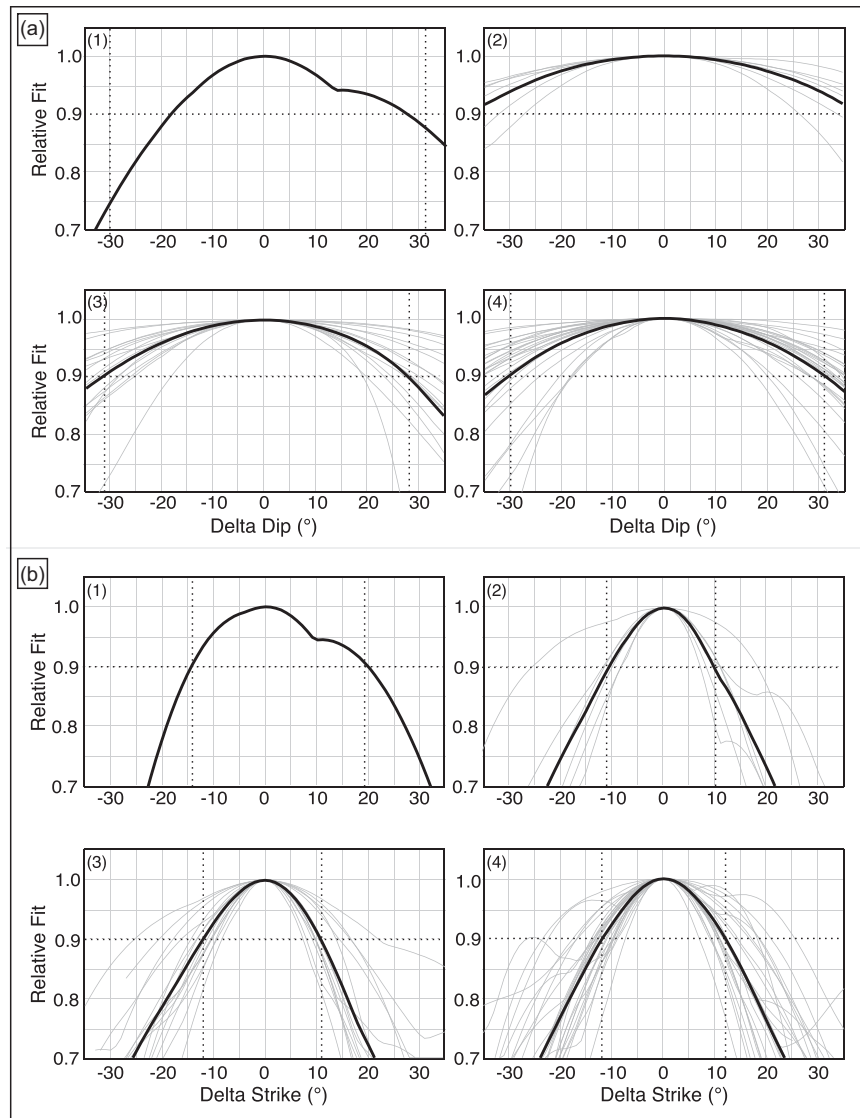
Figure 8. 49 Oklahoma earthquakes with repeatable RMT solutions divided into four groups based on maximum fit: (1) greater than 0.8, (2) 0.7–0.8, (3) 0.6–0.7 and (4) 0.5–0.6. (a) Relative dip and (b) strike are plotted in grey for all events in each group. The thick, solid black lines show the average strike or dip falloff for the respective group. Horizontal dotted black lines show the cut-off for acceptable solutions at 0.9 relative fit. Vertical dotted black lines coincide with the intersection of the acceptable solution and average falloff lines, bounding the average values of delta strike and delta dip (with respect to the best fit of each parameter) that have a relative fit within 90 per cent of the best-fitting solution. Range of acceptable fits is not directly correlated with maximum fit, indicating that uncertainty range is characteristic of the data set, not varying quality of the RMT inversions.

and faulting style, we repeated some of the synthetic tests from Section 2 using station components individually.

First, we revisited how station density affects fit falloff (Section 2) for five hypothetical networks with 3, 4, 12, 24 and 36 stations, respectively, and using only one station component (radial, transverse or vertical). In a second test, we evaluated an RMT from the Oklahoma data set (that which Fig. 14 is based upon), using synthetic data, without noise, at station locations used to compute the real RMT. As in the first test, we ran the inversion with individual station components; however, this test differs because not all components were used at each station for the real RMT, so focal sphere coverage varies among the radial, transverse, and vertical component cases.

Table 2 summarizes the results. If we exclude the four-station network (discussed in Appendix F), the ranges of acceptable strike vary by only $7°$ (ranges of 17–$23°$) among all cases. Thus, the

synthetic test networks and our real network (the combination of stations monitoring the Oklahoma earthquakes) all have sufficient azimuthal coverage to provide strong constraint on strike, regardless of whether a single component or all components are used. On the other hand, the range of acceptable dips varies significantly among the tests, increasing substantially if the transverse component is included. When used alone, the transverse component provides virtually no constraint on dip; the entire range of dips tested yielded relative fits above 0.9. This stems from the uniformity among the synthetic waveform transverse components for each value of dip (Fig. 14), and is consistent with the result from Dufumier & Cara (1995) and Dufumier (1996) that the radiation recorded at stations within $30°$ of each other (or in this case, stations rotating azimuthally by up to only $\sim30°$ from the best-fitting nodal plane) require multiple station components to be distinguishable. On the other hand, the radial and vertical components yield ranges close to the strike
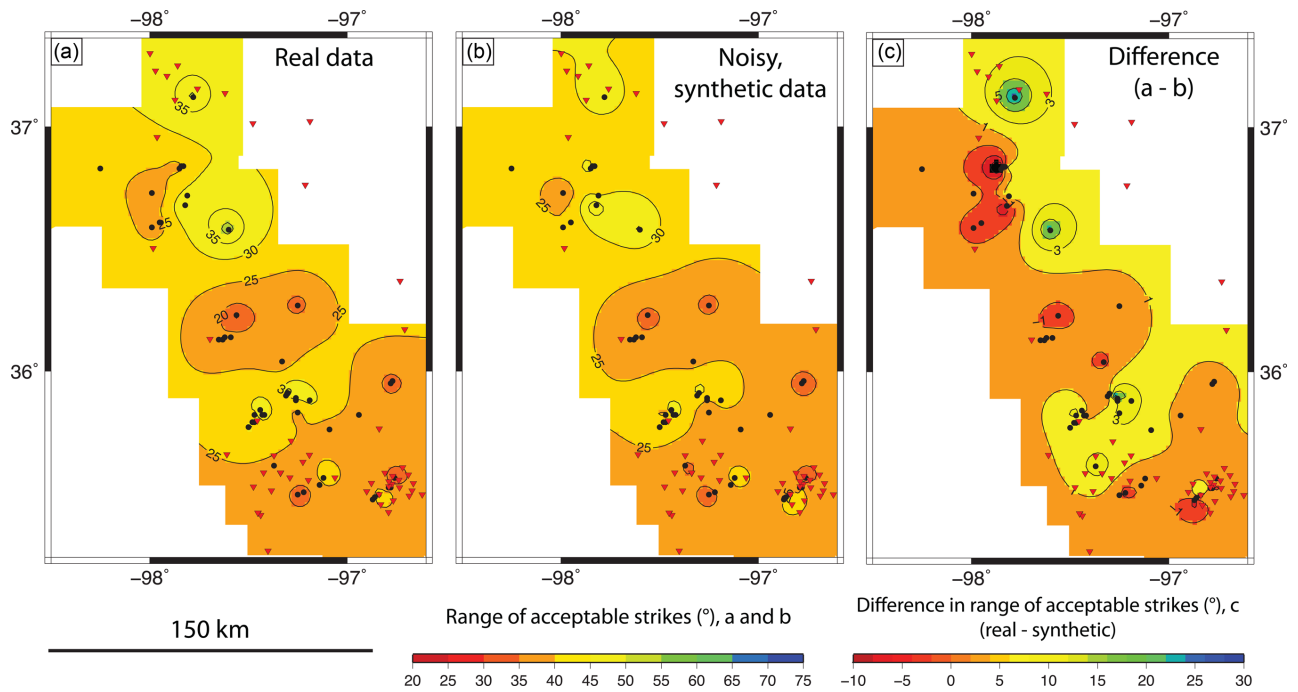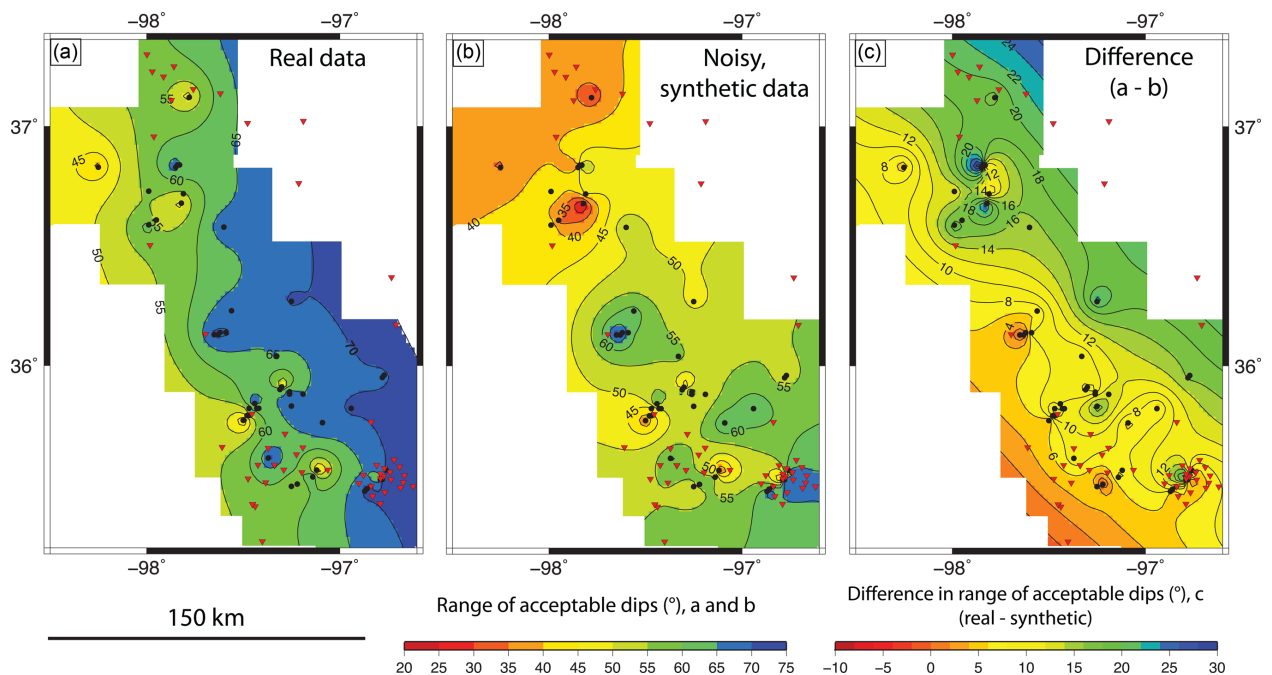
Figure 9. Spatial distribution of range of acceptable strikes for 49 Oklahoma earthquakes, Scenarios 1 and 2. Black dots are earthquake epicentres. Inverted red triangles are station locations. (a) Scenario 1: range of acceptable strikes for RMTs using real data. (b) Scenario 2: range of acceptable strikes for RMTs using synthetic data with noise. (c) Scenario 1 minus Scenario 2: difference in range of acceptable strikes when real versus noisy synthetic data are used. Contour interval for all plots is 5°.

Figure 10. Spatial distribution of range of acceptable dips for 49 Oklahoma earthquakes, Scenarios 1 and 2. Black dots are earthquake epicentres. Inverted red triangles are station locations. (a) Scenario 1: range of acceptable dips for RMTs using real data. (b) Scenario 2: range of acceptable dips for RMTs using synthetic data with noise. (c) Scenario 1 minus Scenario 2: difference in range of acceptable dips when real vs noisy synthetic data are used. Contour interval for all plots is 5°.

ranges (17–23°). For the same networks but using all components, the range of acceptable dips increases to over 50°, illustrating the effect of the transverse component. Using the real events yields similar results; the ranges of acceptable dip for all components or transverse component independently exceed those for the radial and vertical components by more than 15°.

4.4 Comparison to routinely applied RMT robustness tests

Traditional tests to assess inversion-based model robustness include systematic application of statistical jackknifing and bootstrapping. We applied these traditional tests for both test cases to determine
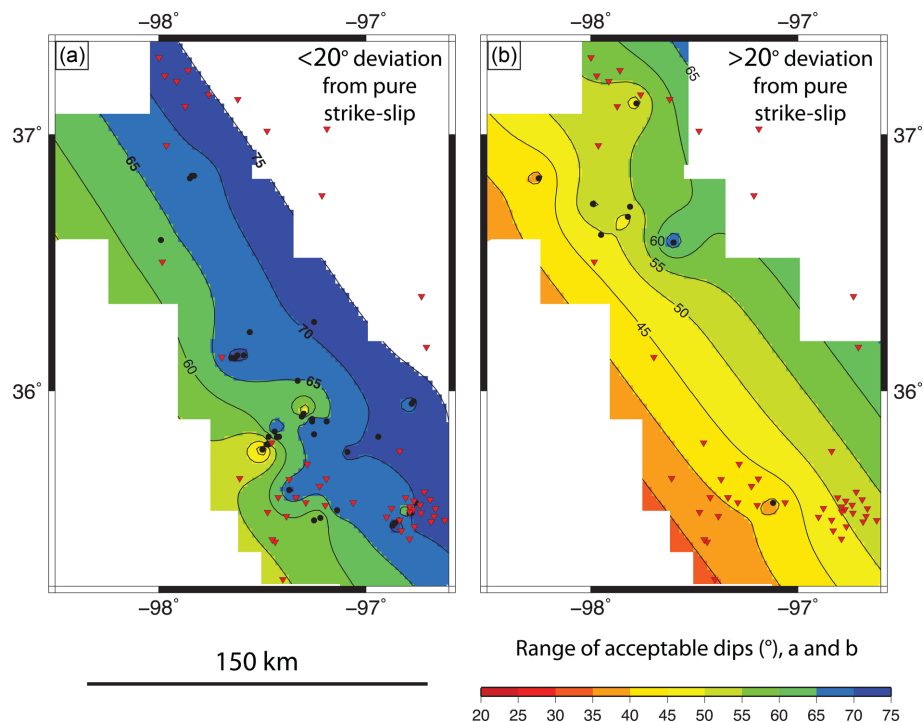
Figure 11. Spatial distribution of range of acceptable dips for 49 Oklahoma earthquakes, divided by rake. Black dots are earthquake epicentres. Inverted red triangles are station locations. (a) Strike-slip earthquakes: range of acceptable dips for RMTs using real data with rake-values less than 20° from pure strike-slip. (b) Dip-slip earthquakes: range of acceptable dips for RMTs using real data with rake-values more than 20° from pure strike-slip. Contour interval for both plots is 5°.
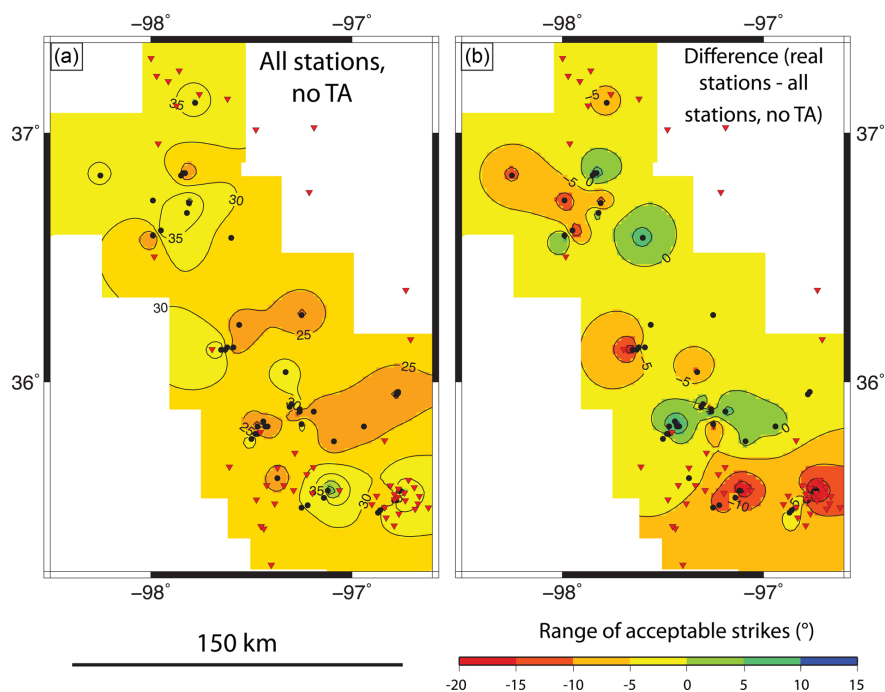

Figure 12. Spatial distribution of range of acceptable strike for 49 Oklahoma earthquakes. (a) Scenario 3: synthetic waveforms with noise for all stations except the Transportable Array. (b) Scenario 3 minus Scenario 2: the difference in range of acceptable strikes computed from synthetic data with noise for only the real stations minus that for all stations but the transportable array. Black dots are earthquake epicentres. Inverted red triangles are station locations. The contour interval is 5°.

whether the contrasting methods suggest comparable moment tensor sensitivities, running the tests for only a subset of data due to computational limitations. We performed 1000 iterations of bootstrapping to 10 per cent of events for both test cases. We also performed jackknifing tests on one event from each test case. The selected Maule aftershock used 20 stations, and we performed jackknifing tests for all station combinations with 80 per cent or more of the stations for a total of 1016 iterations. The selected Oklahoma
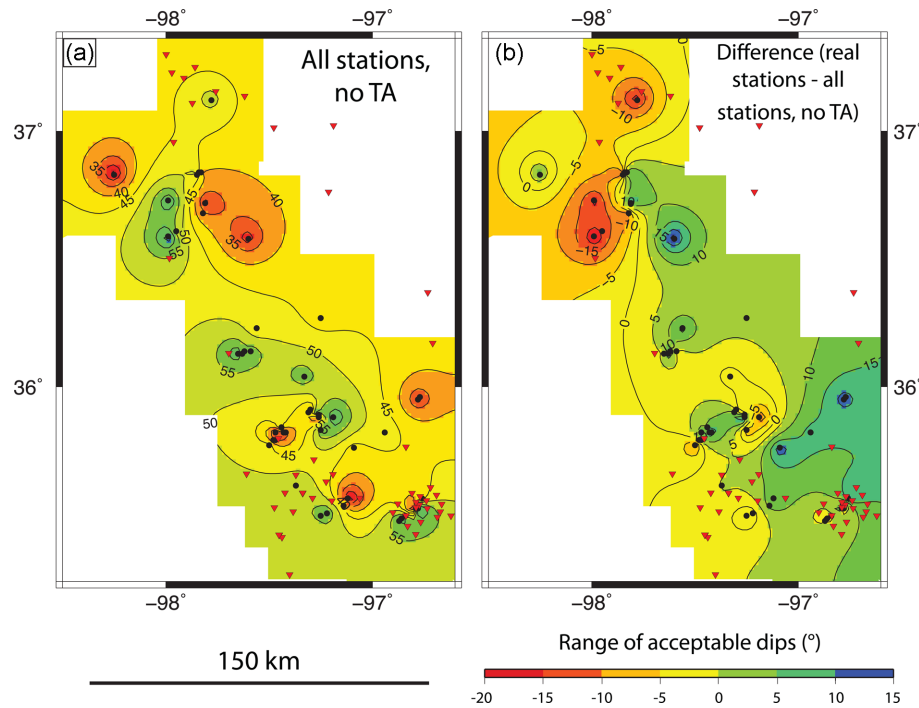
Figure 13. Spatial distribution of range of acceptable dips for 49 Oklahoma earthquakes. (a) Scenario 3: synthetic waveforms with noise for all stations except the Transportable Array. (b) Scenario 3 minus Scenario 2: the difference in range of acceptable dips computed from synthetic data with noise for only the real stations minus that for all stations but the transportable array. Black dots are earthquake epicentres. Inverted red triangles are station locations. The contour interval is 5°.

event used 30 stations, and we performed jackknifing tests for all station combinations with 90 per cent or more of the stations for a total of 456 iterations. We compiled the solutions for each event into 1° bins, and bounded the ranges of acceptable strikes and dips by the highest and lowest bin that comprised at least 1 per cent of the iterations for that event.

Table 3 summarizes the results for the bootstrapping and jackknifing tests, as well as the results using our methodology for both test cases. The results from the three different approaches are qualitatively consistent in that for Maule, strike ranges exceed dip ranges, while for Oklahoma, the dip ranges exceed strike ranges. However, our computed means and the interevent ranges for both test cases and both parameters are much larger. We attribute this partially to our limiting the jackknifing and bootstrapping tests to only a subset of events. Our method is advantageous in that systematic application to large data sets is less computationally intensive than that for jackknifing and bootstrapping, while perhaps providing more conceptually intuitive results.

5 DISCUSSION

In this paper, we quantified how regional station distribution affects the sensitivity of RMT focal mechanism parameters (strike and dip) computed by inverting waveform time-series based on the method of Herrmann *et al.* (2011a). We observed how small changes to strike or dip affected the data-model fit of RMT inversions. We observed a parameter space of 35° in each direction of the best-fitting strike and dip computed by the RMT inversion, and chose a relative fit value of 0.9 as the cut-off for 'acceptable' solutions, and then used the range of acceptable fits to reflect on the sensitivity of the RMT.

We applied our analysis to two sets of earthquake RMTs: (1) the aftershock sequence of the 2010 Maule earthquake, monitored by

the IMAD network; and (2) the ongoing sequence of earthquakes in Oklahoma and southern Kansas, monitored by local, regional, and national temporary and permanent deployments. These two data sets differed in that (1) was dominated by dip-slip RMTs and monitored only ~50 per cent azimuthally by seismic stations, while (2) was dominated by strike-slip RMTs with more complete azimuthal coverage. Additionally, the RMTs in (1) had larger (and a larger span of) magnitudes and depths than those in (2).

We found that in addition to azimuthal coverage, faulting mechanism affects RMT sensitivity. Dip was better constrained for the dip-slip Maule RMTs, while strike was better constrained for the strike-slip Oklahoma RMTs. Based on our initial hypothesis that station distribution has the largest impact on RMT sensitivity, this result was surprising. We focus on the following two points.

(1) Most of the Oklahoma and southern Kansas earthquakes had complete or near-complete azimuthal coverage, while the Maule aftershocks that predominantly occurred offshore were recorded only by stations along the Chilean coast, thus leaving a ~180° azimuthal gap for most events, and larger gaps for those offshore or in the south. While the Oklahoma network better-constrained strike, the RMT fit for most Oklahoma earthquakes was almost completely insensitive to changes in dip. Thus, azimuthal coverage alone cannot be expected to improve dip constraint; other parameters such as magnitude, depth, and mechanism may play into RMT sensitivity (this is partially addressed by the second result). This result is important when RMTs compose the framework of a study, such as resolving the directions of regional compressive stresses contributing to fault failure, especially where large earthquakes occur infrequently; interpreting the dimensions and orientations of subsurface faults that contribute to seismic hazard; and assessing the interactions among faulting events in an earthquake sequence (such
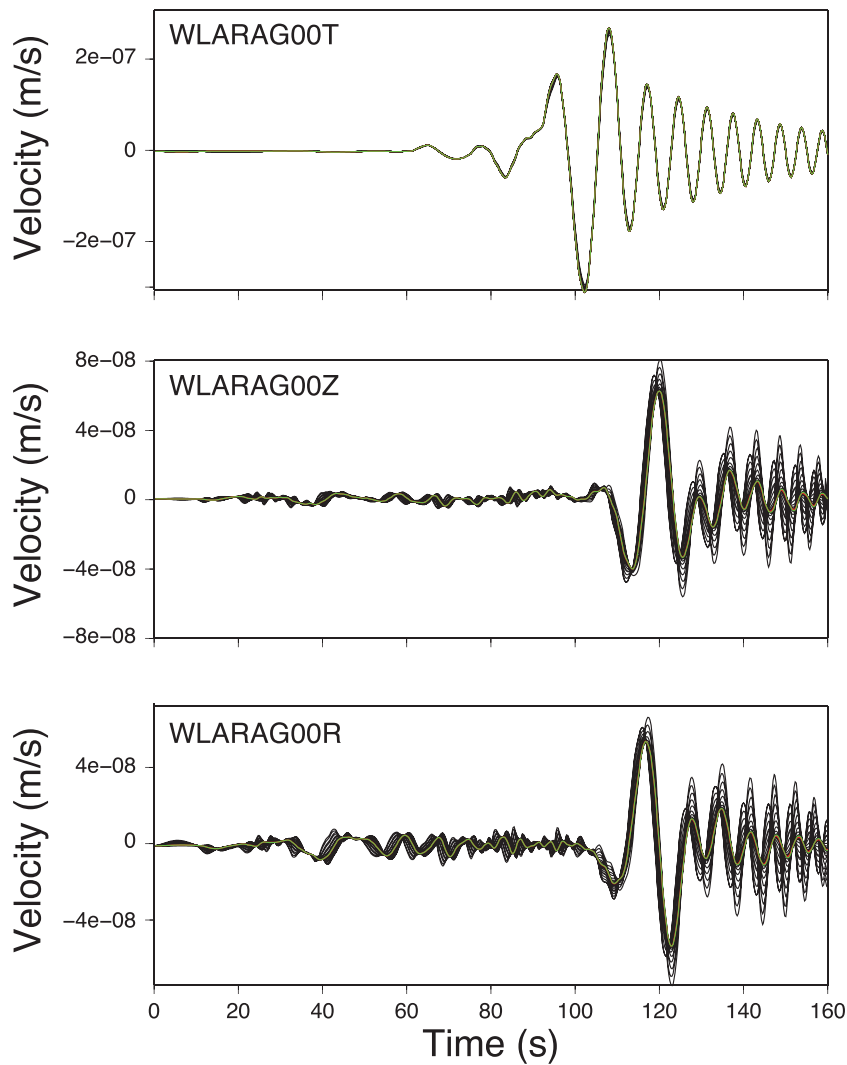
Figure 14. Synthetic waveforms (no noise) produced for a station azimuthally aligned with one nodal plane of an Oklahoma earthquake RMT: transverse component (top), vertical component (middle) and radial component (bottom). The grey line represents the RMT solution, and the black lines are waveforms when the dip is rotated from the best-fitting dip by ±1°, 2°, 4°, 7°, 11°, 16°, 21°, 26°, 31° and 36°.

Table 2. Ranges of strike and dip computed when synthetic seismograms for each of the R-, T- and Z-components, as well as all components are used in several hypothetical test cases and for a real event.

	Range (°) R-component		Range (°) T-component		Range (°) Z-component		Range (°) All-components	
Test	Strike	Dip	Strike	Dip	Strike	Dip	Strike	Dip
3 stations	21	22	17	>70	21	23	17	52
4 stations	>70	29	1	7	>70	29	7	27
12 stations	19	21	19	>70	19	21	19	55
24 stations	19	21	19	>70	19	21	19	55
36 stations	21	21	19	>70	21	21	19	57
Real event	22	45	22	>70	23	55	21	>70

as through Coulomb stress transfer). For example, McNamara *et al.* (2015b) used RMTs to interpret the subsurface Wilzetta-Whitehorse fault zone near Cushing, Oklahoma as active and potentially hazardous to local communities; the fault plane geometry of recent earthquakes affects whether these faults have become closer to or pushed farther from failure.

(2) While most of the Oklahoma RMTs were dominated by a strike-slip sense of motion, a few had large normal components,

and this allowed us to consider style of faulting in our analysis. All but one of the Oklahoma RMTs that had a ≥20° dip-slip component had a range of acceptable dips well below the mean value for the full data set. The same pattern, however, did not appear in the Maule aftershock data set; no dichotomy existed in range of acceptable dips between the strike-slip and dip-slip earthquakes. We speculate that this dependency may be a function of source depth; Oklahoma earthquakes were shallow, mostly above 5 km depth, while Maule

Table 3. Ranges of strike and dip computed for the Maule and Oklahoma test cases using real and synthetic data, and from the bootstrapping and jackknifing tests.

		Maule		Oklahoma	
		Strike	Dip	Strike	Dip
Real	Range	9° to >71°	18° to >71°	14° to 44°	38° to >71°
	Mean	56°	44°	26°	60°
Synthetic	Range	20° to 62°	20° to 60°	17° to 44°	22° to >71°
	Mean	46°	31°	25°	52°
Bootstrapping	Range	6° to 36°	4° to 30°	8° to 35°	19° to 60°
	Mean	22°	11°	19°	39°
Jackknifing		18°	9°	6°	28°

aftershocks were closer to 20 km or more. This result may indicate that the effect of faulting style on RMT sensitivity is exaggerated for shallow hypocentres. Seismic monitoring in the central and eastern United States is affected by this result, since the thin, stable crust hosts shallow earthquakes (mostly <10 km depth).

An unexpected result arising from our study relates to data quality. Depending on faulting mechanism, some station components degrade rather than enhance RMT quality; that is, including some station components in the RMT inversions increased ambiguity. Here, we focused on strike-slip faulting, based on the surprisingly large range of acceptable dips observed for most Oklahoma earthquake RMTs. Our fit sensitivity analysis using synthetic single-component records revealed that the transverse component is virtually indistinguishable over a broad range of dip, and therefore the RMTs were completely insensitive to this component. By including only the vertical and radial components in the inversions, we greatly decreased the range of acceptable dips. On the other hand, the transverse component was still useful in computing a well-constrained strike value. Thus, we suggest that more rigorous data selection combined with variable weighting could improve our ability to compute well-constrained RMTs inversions (e.g. weighting station components in addition to epicentral distance when solving for each parameter).

6 CONCLUSIONS

We inverted real and synthetic time-series velocity waveforms to compute RMT solutions for 293 Maule aftershocks and 49 Oklahoma and southern Kansas earthquakes. We calculated the relative fits for a broad range of strikes and dips for each earthquake, and observed the following ranges of acceptable strike and dip:

Maule, real – strike: 9° to >71°, average 56°; dip: 18° to >71°, average 44°.
Maule, synthetic – strike: 20° to 62°, average 46°; dip: 20° to 60°, average 31°.
Oklahoma, real – strike: 14° to 44°, average 26°; dip: 38° to >71°, average 60°.
Oklahoma, synthetic – strike: 17° to 44°, average 25°; dip: 22° to >71°, average 52°.

We draw two main conclusions from this study. (1) While station distribution does have an impact on our ability to constrain RMTs using waveform time-series, faulting style also plays a role and (2) increased station density and data quantity does not necessarily improve RMT constraint. This information is perhaps useful for future network deployments; the optimal way to expend resources (i.e. distribute seismometers) may depend on the tectonic setting, and the depth and type of faulting expected. For example, station density could be increased along the anticipated strikes of the nodal planes (e.g. north–south for the Maule aftershocks) to improve strike constraint. In turn, stations could be thinned in other azimuthal directions, while maintaining variable (anticipated) source-station distance to avoid redundant stations at which similar waveforms would result for a wide range of strikes or dips. Importantly, however, if computing non-double-couple moment tensor components in addition to fault geometry and slip direction, these stations are most sensitive to 3-D wave propagation effects. A second potential use for these results is to guide a more rigorous selection process for input data into RMT inversion. For example, all stations could be used initially, but then those azimuthally far from the nodal planes removed to improve strike constraint. In another example, transverse components could be eliminated to compute dip for earthquakes expected to occur on steeply dipping fault planes with strike slip motion. A third possibility is to use the methodology described here to identify candidate earthquakes with better constraint for applications in which high uncertainties could largely impact the results (e.g. determining stress orientations). Finally, our study implies that exploring variable weighting among stations used in RMT inversions may help to improve fault geometry constraint.

REFERENCES

Beck, S. *et al.*, 2014. Advancing subduction zone science after a big quake, *EOS, Trans. Am. geophys. Un.*, **95**(23), 193, doi:10.1002/2014EO23.

Braunmiller, J., Dahm, T. & Bonjer, K.P., 1994. Source mechanism of the 1992 Roermond earthquake from surface-wave inversion of regional data, *Geophys. J. Int.*, **116**(3), 663–672.

Braunmiller, J., Kradolfer, U., Baer, M. & Giardini, D., 2002. Regional moment tensor determination in the European–Mediterranean area—initial results, *Tectonophysics*, **356**(1), 5–22.

Crotwell, H.P., Owens, T.J. & Ritsema, J., 1999. The TauP toolkit: flexible seismic travel-time and ray-path utilities, *Seismol. Res. Lett.*, **70**(2), 154–160.

Dufumier, H., 1996. On the limits of linear moment tensor inversion of teleseismic body wave spectra, *Pure appl. Geophys.*, **147**(3), 467–482.

Dufumier, H. & Cara, M., 1995. On the limits of linear moment tensor inversion of surface wave spectra, *Pure appl. Geophys.*, **145**(2), 235–257.

Farr, T.G. *et al.*, 2007. The shuttle radar topography mission, *Rev. Geophys.*, **45**(2), doi:10.1029/2005RG000183.

Ford, S.R., Douglas, S.D. & Walter, W.R., 2009. Identifying isotropic events using a regional moment tensor inversion, *J. geophys. Res.: Solid Earth*, **114**(B1), doi:10.1029/2008JB005743.

Giardini, D., Boschi, E. & Palombo, B., 1993. Moment tensor inversion from Mednet data (2) Regional earthquakes of the Mediterranean, *Geophys. Res. Lett.*, **20**(4), 273–276.

Hayes, G.P., Bergman, E., Johnson, K.L., Benz, H.M., Brown, L. & Meltzer, A.S., 2013. Seismotectonic framework of the 2010 February 27 M_{w} 8.8 Maule, Chile earthquake sequence, *Geophys. J. Int.*, **195**(2), 1034–1051.

Herrmann, R.B., Ammon, C.J. & Koper, K.D., 2004. GSAC-generic seismic application computing, in *Proceedings of the AGU Fall Meeting* Abstracts, Vol. 1, 273 pp.

Herrmann, R.B., Malagnini, L. & Munafò, I., 2011a. Regional moment tensors of the 2009 L'Aquila earthquake sequence, *Bull. seism. Soc. Am.*, **101**(3), 975–993.

Herrmann, R.B., Benz, H. & Ammon, C.J., 2011b. Monitoring the earthquake source process in North America, *Bull. seism. Soc. Am.*, **101**(6), 2609–2625.

Kanamori, H. & Rivera, L., 2008. Source inversion of W phase: speeding up seismic tsunami warning, *Geophys. J. Int.*, **175**, 222–238.

Keranen, K., 2011. *Oklahoma RAMP, International Federation of Digital Seismograph Networks*, other/seismic Network, doi:10.7914/SN/ZQ_2011.

McNamara, D.E., Benz, H.M., Herrmann, R.B., Bergman, E.A., Earle, P., Holland, A., Baldwin, R. & Gassner, A., 2015a. Earthquake hypocenters and focal mechanisms in central Oklahoma reveal a complex system of reactivated subsurface strike-slip faulting, *Geophys. Res. Lett.*, **42**(8), 2742–2749.

McNamara, D.E. *et al.*, 2015b. Reactivated faulting near Cushing, Oklahoma: increased potential for a triggered earthquake in an area of United States strategic infrastructure, *Geophys. Res. Lett.*, **42**, 8328–8332.

Michele, M., Custódio, S. & Emolo, A., 2014. Moment tensor resolution: case study of the Irpinia seismic network, Southern Italy, *Bull. seism. Soc. Am.*, **104**(3), 1348–1357.

Nabelek, J. & Xia, G., 1995. Regional and teleseismic analysis of the 29 March, 1993. Scotts Mills, Oregon, earthquake, *Geophys. Res. Lett.*, **22**, 13–16.

Pesicek, J.D., Sileny, J., Prejean, S.G. & Thurber, C.H., 2012. Determination and uncertainty of moment tensors for microearthquakes at Okmok Volcano, Alaska, *Geophys. J. Int.*, **190**(3), 1689–1709.

Peterson, J., 1993. Observations and modeling of seismic background noise, *U.S. Geol. Surv. Open File Rep.*, Vol. 93–322.

Ristau, J., Rogers, G.C. & Cassidy, J.F., 2007. Stress in western Canada from regional moment tensor analysis, *Can. J. Earth Sci.*, **44**(2) 127–148.

Ritsema, J. & Lay, T., 1993. Rapid source mechanism determination of large ($M_{\mathrm{W}} \geq 5$) earthquakes in the western United States, *Geophys. Res. Lett.*, **20**(15), 1611–1614.

Robinson, D.P. & Cheung, L.T., 2010. Source process of the M_{w} 8.3, 2003 Tokachi-Oki, Japan earthquake and its aftershocks, *Geophys. J. Int.*, **181**, 334–342.

Romanowicz, B., Dreger, D., Pasyanos, M. & Uhrhammer, R., 1993. Monitoring of strain release in central and northern California using broadband data, *Geophys. Res. Lett.*, **20**(15), 1643–1646.

Šílený, J., Campus, P. & Panza, G.F., 1996. Seismic moment tensor resolution by waveform inversion of a few local noisy records—I. Synthetic tests, *Geophys. J. Int.*, **126**(3), 605–619.

Stich, D., Ammon, C.J. & Morales, J., 2003. Moment tensor solutions for small and moderate earthquakes in the Ibero-Maghreb region, *J. geophys. Res.: Solid Earth*, **108**(B3), doi:10.1029/2002JB002057.

UC San Diego, 2013. Central and Eastern US Network. International Federation of Digital Seismograph Networks, Other/Seismic Network, doi:10.7914/SN/N4.

USGS National Earthquake Information Center (NEIC), 1990. United States National Seismic Network, International Federation of Digital Seismograph Networks, Other/Seismic Network, doi:10.7914/SN/US.

Wessel, P. & Smith, W.H.F., 1991. Free software helps map and display data, *EOS, Trans. Am. geophys. Un.*, **72**(441), 445–446.

Zahradník, J. & Custódio, S., 2012. Moment tensor resolvability: application to Southwest Iberia, *Bull. seism. Soc. Am.*, **102**(3), 1235–1254.

APPENDIX A: METHODOLOGY

A.1 RMT inversion and range of acceptable fits computation

All RMTs here are computed according to the time-series waveform inversion of Herrmann *et al.* (2011b). The inversion determines the best-fitting focal mechanism by comparing the observed velocity waveforms (in this case, the synthetic waveforms) to the computed Green's functions for each solution within a solution space. The input and computed waveforms are cut and filtered using the same bounds, and waveforms are weighted according to a step-wise function of distance.

We configure the inversion to search through the solution space in three phases. Initially, we define the solution space as a 10° step through all possible strike-, dip- and rake-values, computing the fit-value for each combination of these three parameters, while holding hypocentral latitude, longitude and depth constant according to our predefined and relocated focal mechanisms. Next, we refine the grid search to 1° increments surrounding the best-fitting solution from the initial solution space. Finally, we compute the fit-value of each incremental strike or dip within 35° of that focal mechanism (resolved to the nearest 1°) while holding all other parameters constant, and retain solutions that we deemed 'acceptable' to include in further analysis.

Here, 'acceptable' is defined as any focal mechanism with a relative fit value 90 per cent or greater than that for the best-fitting RMT. To choose the threshold of 90 per cent, we closely inspected synthetic seismograms produced for a wide range of strikes and dips, and identified the delta strike and dip that revealed a distinct change in either the shape or amplitude of the waveform. We then computed the relative fit for the identified delta strike and dip using synthetic seismograms. This definition of 'acceptable' is used for all tests included in this study. For each test, we discuss the range of acceptable values, meaning the number of acceptable solutions spanning the total ± strike or dip model space.

We use the same inversion and analysis processes for all tests in this study; however, when real data are used, we include a few a
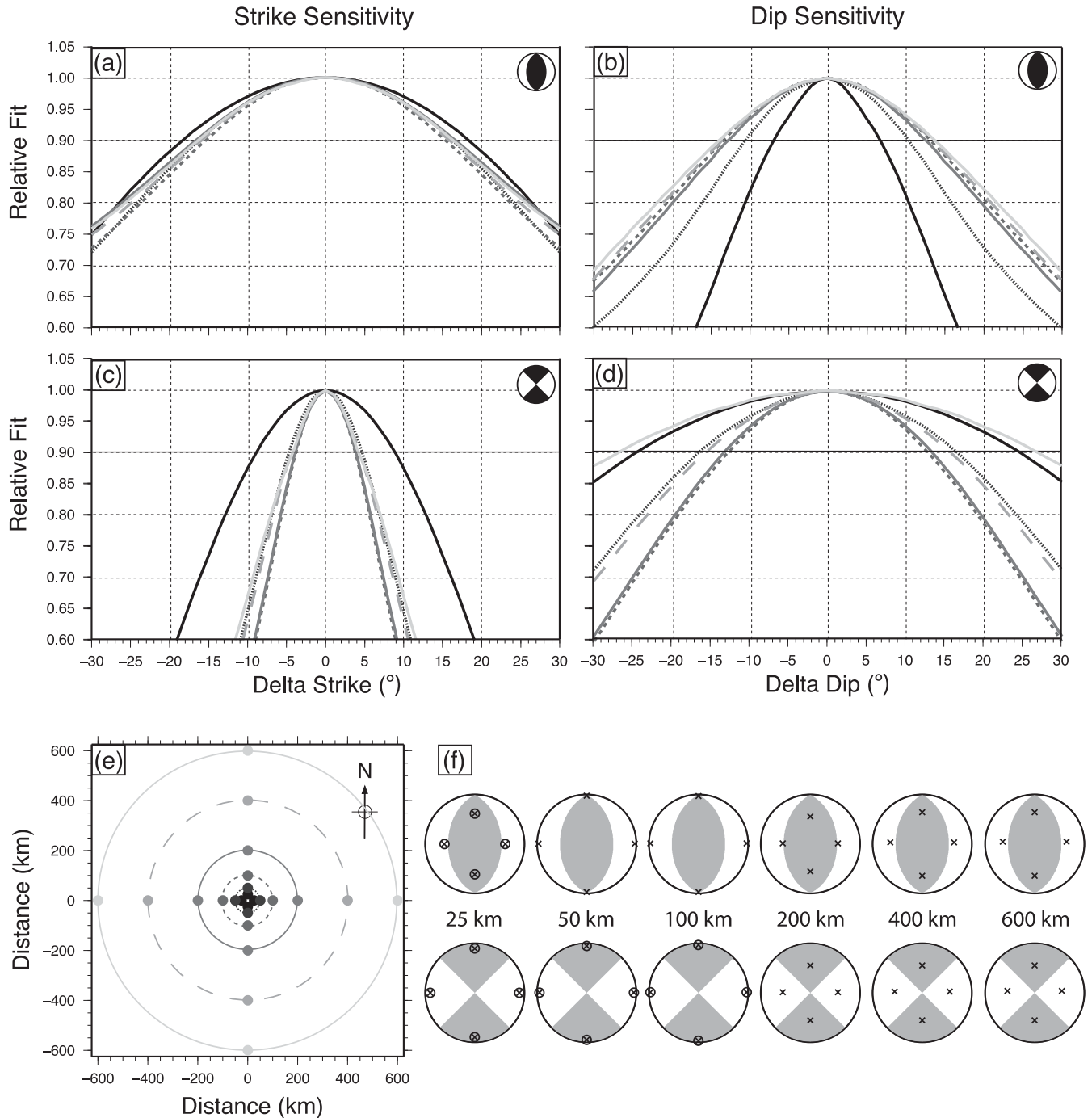
Figure A1. RMT sensitivity to change in event-station distance for a thrust (strike/dip/rake = 0°/45°/90°, depth = 20 km, M_W = 4.0) and strike slip mechanism (strike/dip/rake = 315°/90°/0°, depth = 5 km, M_W = 4.0). Stations are spaced azimuthally by 90°, with the first station placed due north. (a) Strike sensitivity, reverse mechanism. (b) Dip sensitivity, reverse mechanism. (c) Strike sensitivity, strike-slip mechanism. (d) Dip sensitivity, strike-slip mechanism. (e) Station distribution about the earthquake sources; filled circles are station locations. The source is at (0, 0). (f) Focal mechanisms with locations of first motions for each station, text indicates distance. An X represents a down-going first arrival and a circled X represents an upgoing first arrival. Take-off angle of the first motion is computed using TauP (Crotwell *et al.* 1999). Note that first motions plot in different positions for same depths but different mechanisms because take-off angle depends on both source-station distance and depth. Curve colours and patterns in (a), (b), (c) and (d) correspond to the like colour for station distance in (e). The solid black horizontal line indicates a relative fit value of 0.9; the part of each curve that plots above this line represents the range of acceptable fits.

few additional steps prior to the inversion. We first perform quality control. We examine the rotated traces for all available broad-band stations within 600 km of the epicentre, at this stage cut from −10 to 180 s with respect to the *P*-wave arrival and filtered with high-pass

0.02 Hz and low-pass 0.10 Hz three-pole causal Butterworth filters, choosing the successfully rotated velocity records with good signal to noise ratio. Next, we run an initial iteration of the inversion. Based on the results, we adjust the following inversion configurations:
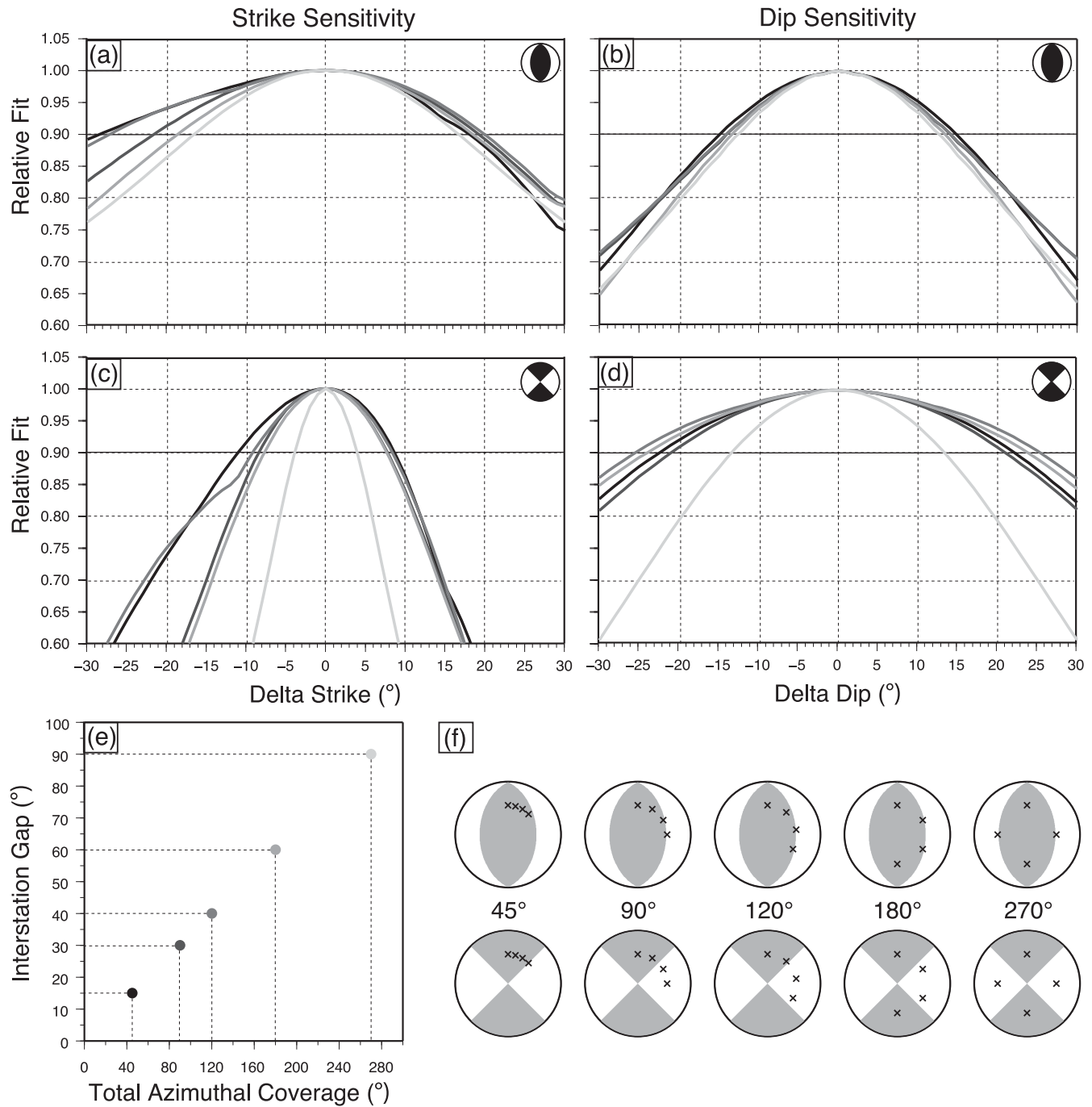
Figure A2. RMT sensitivity to changing focal sphere coverage, with the first station always aligned due north, and four stations at 200 km epicentral distance spaced equally within a specified azimuthal range, for a thrust (strike/dip/rake $= 0°/45°/90°$, depth $= 20$ km, $M_W = 4.0$) and strike slip mechanism (strike/dip/rake $= 315°/90°/0°$, depth $= 5$ km, $M_W = 4.0$). (a) Strike sensitivity, reverse mechanism. (b) Dip sensitivity, reverse mechanism. (c) Strike sensitivity, strike-slip mechanism. (d) Dip sensitivity, strike-slip mechanism. (e) Azimuthal coverage versus interstation gap; a network with less azimuthal coverage has a smaller interstation gap. (f) Focal mechanisms with locations of first motions for each station for each orientation. Take-off angle of the first motion is computed using TauP (Crotwell *et al.* 1999). Text indicates range of azimuthal coverage. Curve colours in (a), (b), (c) and (d) correspond to the like colour for network coverage in (e). The solid black horizontal line indicates a relative fit value of 0.9; the portion of each curve that plots above this line represents the range of acceptable fits.

(1) cutting times, chosen to maximize the amount of signal contained in all selected traces; (2) range of the frequency band used to fit the ground velocity, remaining within the range of 0.02–0.10 Hz but varying among events; and (3) use—or not—of a microseism rejection for frequencies in the range of 0.12–0.25 Hz. Additionally, we remove bad traces. We repeat this process until an acceptable data-model fit is achieved. The inversion process is described in detail in Herrmann *et al.* (2011a).
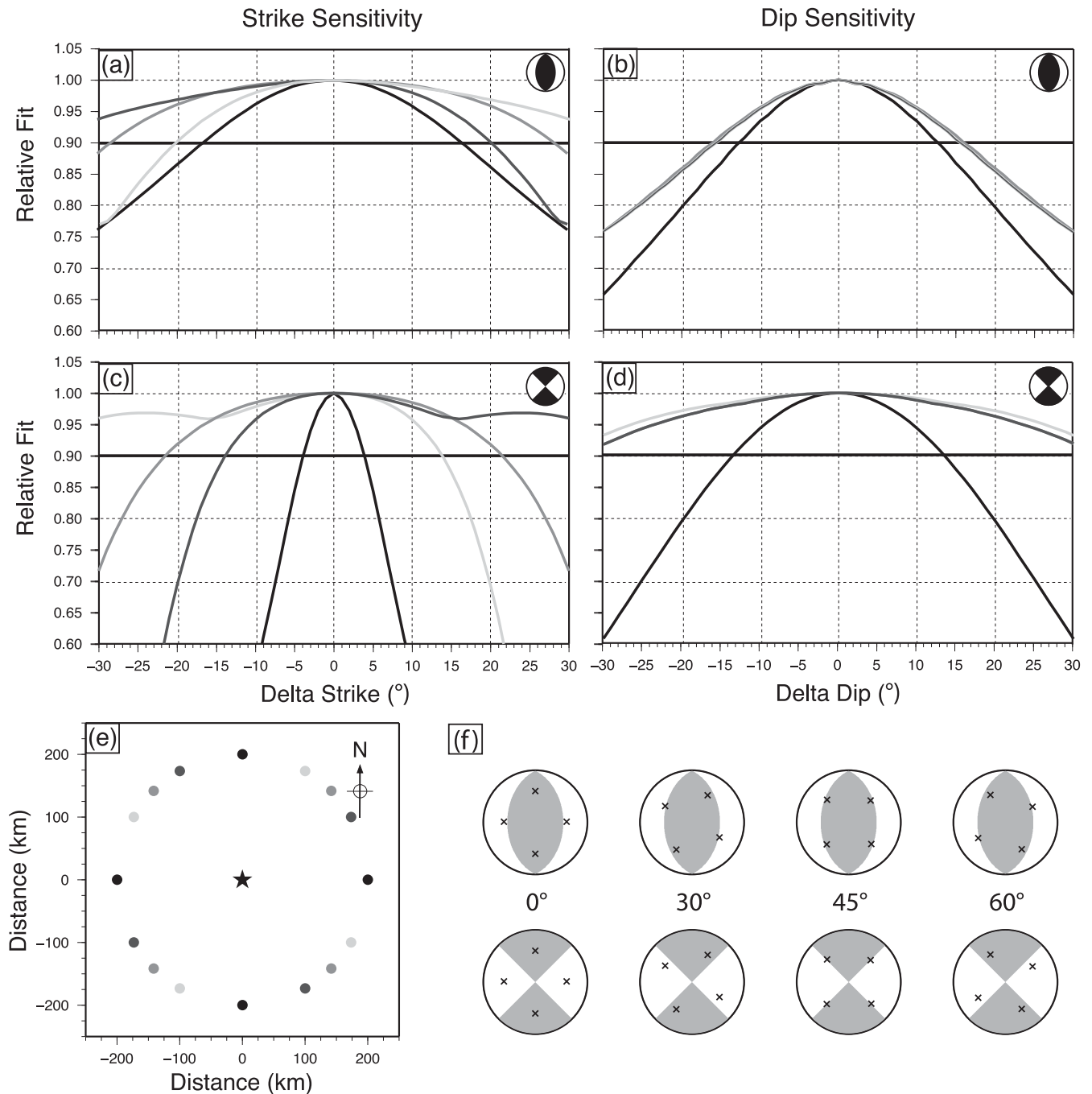
Figure A3. RMT sensitivity to change in event-station azimuth for a thrust (strike/dip/rake = 0°/45°/90°, depth = 20 km, M_W = 4.0) and strike slip mechanism (strike/dip/rake = 315°/90°/0°, depth = 5 km, M_W = 4.0). Four evenly spaced seismometers at 200 km from the earthquake epicentre are rotated azimuthally about the earthquake source. (a) Strike sensitivity, reverse mechanism. (b) Dip sensitivity, reverse mechanism. (c) Strike sensitivity, strike-slip mechanism. (d) Dip sensitivity, strike-slip mechanism. (e) Station distribution about the earthquake sources; the star represents the location of the source relative to stations at each network orientation. (f) Focal mechanisms with locations of first motions for each station. Take-off angle of the first motion is computed using TauP (Crotwell *et al*. 1999). Text indicates orientation in terms of rotation angle of the network from due north. Curve colours in (a), (b), (c) and (d) correspond to the like colour for the network orientation in (e). The solid black horizontal line indicates a relative fit value of 0.9; the portion of each curve that plots above this line represents the range of acceptable fits.
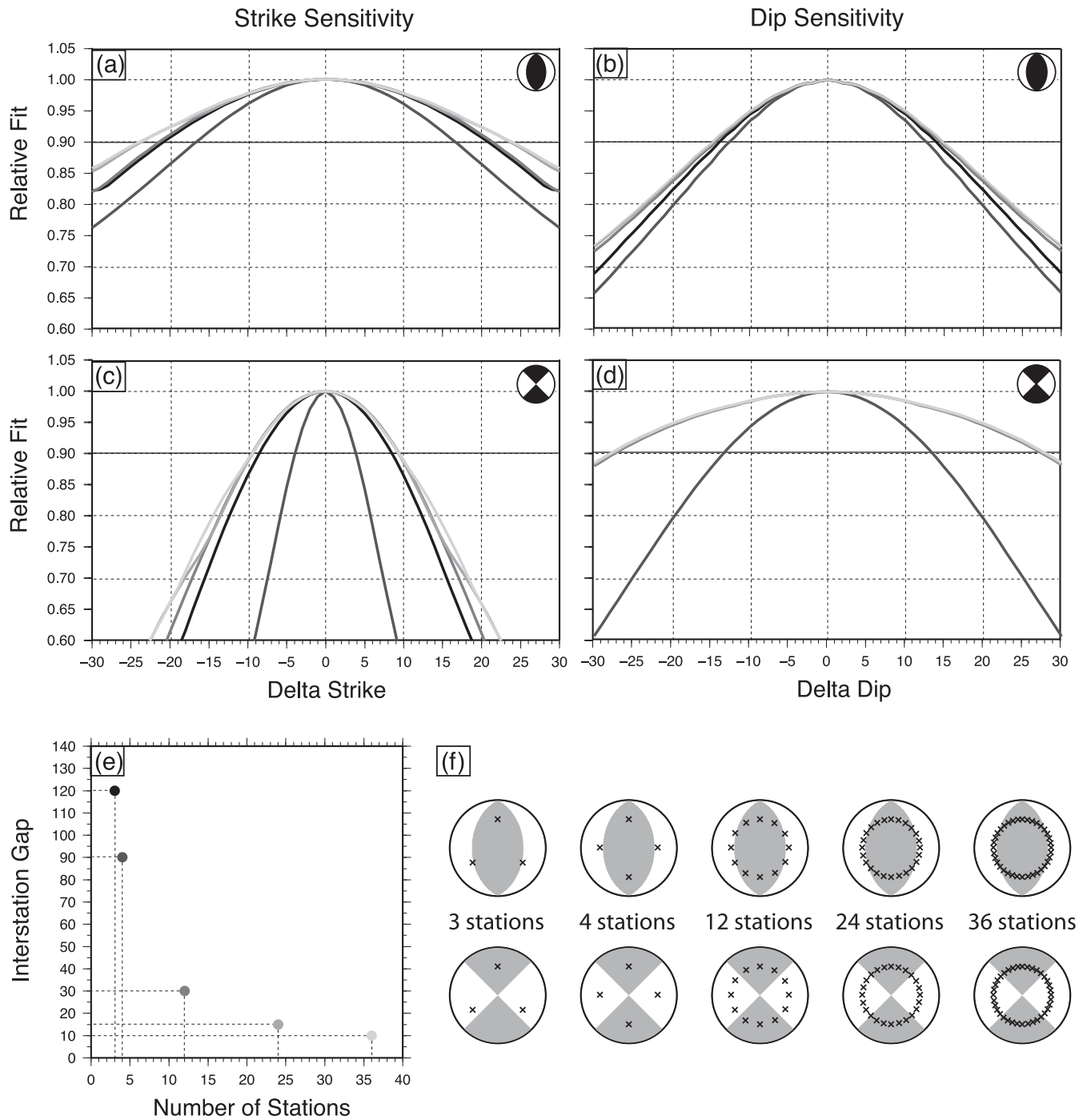
Figure A4. RMT sensitivity to changing station density, with the first station always aligned due north and stations at 200 km epicentral distance spaced equally azimuthally about the epicentre, for a thrust (strike/dip/rake = 0°/45°/90°, depth = 20 km, M_W = 4.0) and strike slip mechanism (strike/dip/rake = 315°/90°/0°, depth = 5 km, M_W = 4.0) (a) Strike sensitivity, reverse mechanism. (b) Dip sensitivity, reverse mechanism. (c) Strike sensitivity, strike-slip mechanism. (d) Dip sensitivity, strike-slip mechanism. (e) Number of stations versus interstation gap; a network with more stations has a smaller interstation gap. (f) Focal mechanisms with locations of first motions for each station. Take-off angle of the first motion is computed using TauP (Crotwell *et al.* 1999). Text indicates number of stations. Curve colours in (a), (b), (c) and (d) correspond to the like colour for network density in (e). The solid black horizontal line indicates a relative fit value of 0.9; the portion of each curve that plots above this line represents the range of acceptable fits.
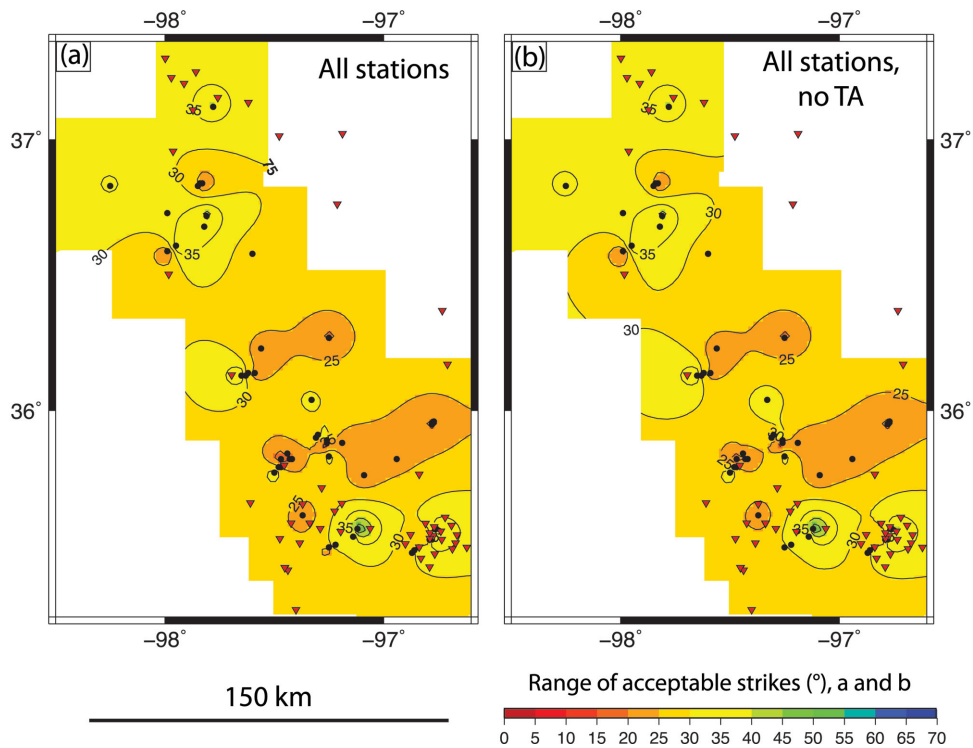
Figure A5. Spatial distribution of range of acceptable strikes for 49 Oklahoma earthquakes, Scenarios S1 and 3. Black dots are earthquake epicentres. Inverted red triangles are station locations. Black dots are earthquake epicentres. Inverted red triangles are station locations. The thick black line is the coastline of Chile. (a) Scenario S1: range of acceptable strikes when synthetic data for all temporary and permanent stations deployed at any time during the study period are included in the RMT inversions. (b) Scenario 3: range of acceptable strikes when synthetic data for all temporary and permanent stations except those from the Transportable Array are included in the RMT inversions. Contour interval for both plots is 5°.
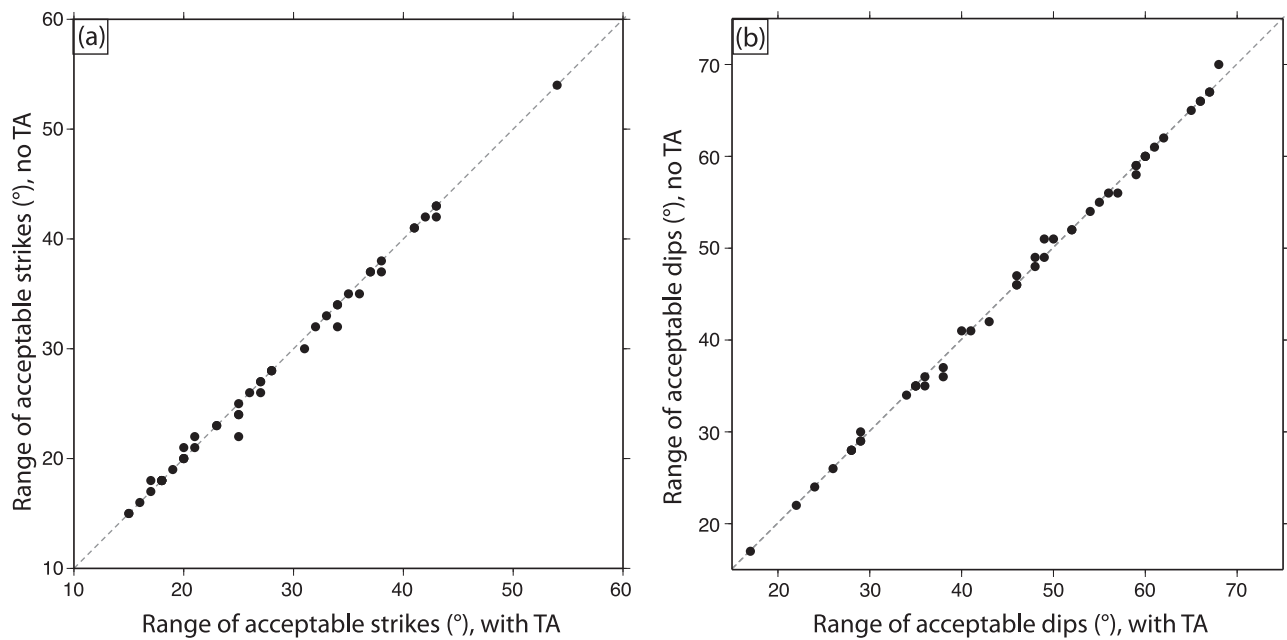
Figure A6. Range of acceptable strikes for synthetic data with noise produced for all stations (Scenario S1) versus all stations except the Transportable Array (Scenario 3). Black dots are ranges for individual RMTs. Dashed grey line is the function $y = x$. Dotted grey lines are offset from $y = x$ by 10°.
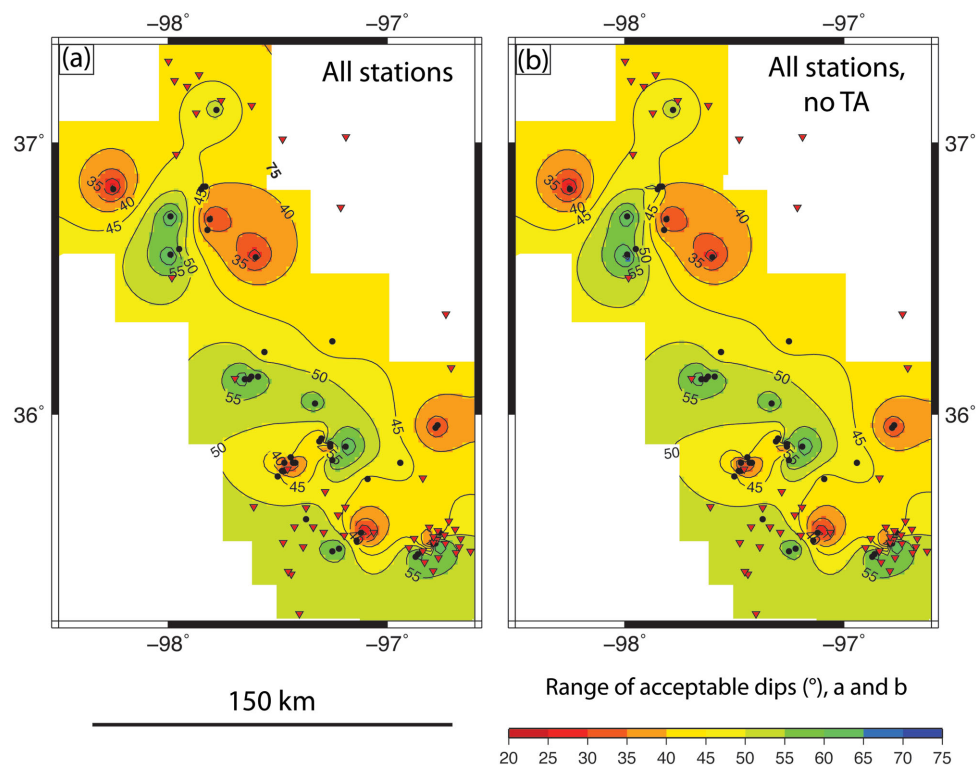
Figure A7. Spatial distribution of range of acceptable dips for 49 Oklahoma earthquakes, Scenarios S1 and 3. Black dots are earthquake epicentres. Inverted red triangles are station locations. The thick black line is the coastline of Chile. (a) Scenario S1: range of acceptable dips when synthetic data for all temporary and permanent stations deployed at any time during the study period are included in the RMT inversions. (b) Scenario 3: range of acceptable dips when synthetic data for all temporary and permanent stations except those from the Transportable Array are included in the RMT inversions. The contour interval is 5°.

Figure A8. Range of acceptable (a) strikes and (b) dips using real data plotted against those using synthetic data with noise for the same stations. Each black dot represents an individual Maule aftershock RMT. Dashed grey line is the function $y = x$. Dotted grey lines are offset from $y = x$ by 10°.

Figure A9. Range of acceptable (a) strikes and (b) dips using synthetic data with noise for stations used in the real inversion plotted against those computed when all IMAD stations were used. Each black dot represents an individual RMT. Dashed grey line is the function $y = x$. Dotted grey lines are offset from $y = x$ by $10°$.
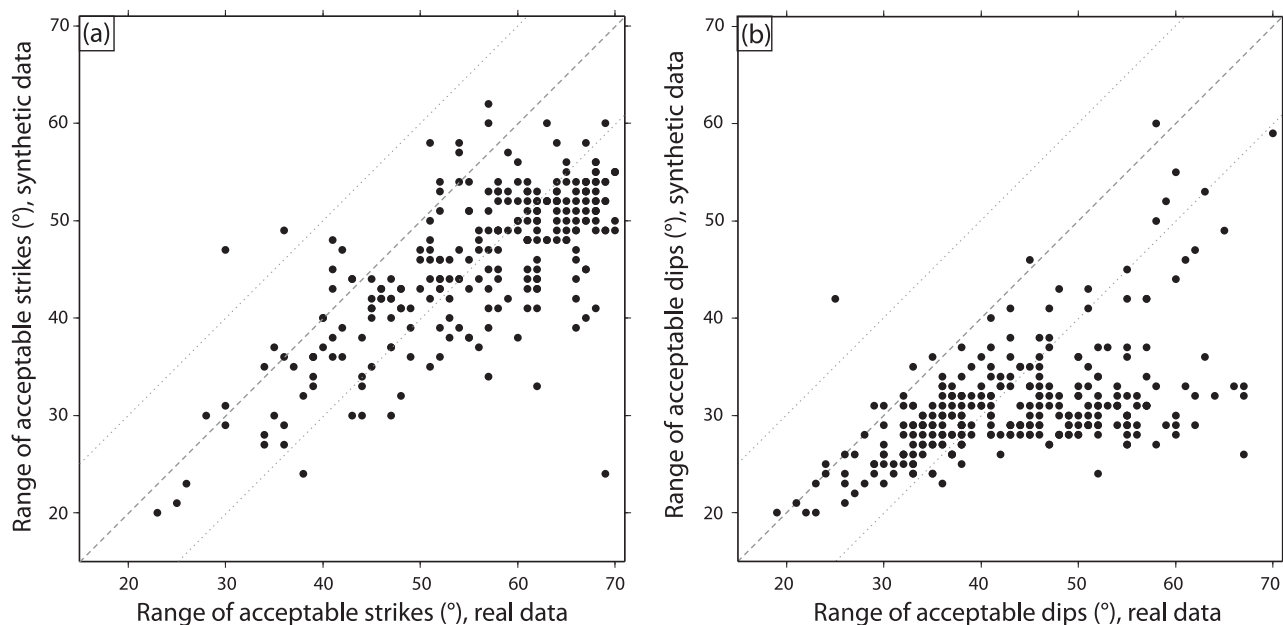

Figure A10. Range of acceptable (a) strikes and (b) dips using real data plotted against those using synthetic data with noise for the same stations. Each black dot represents an individual Oklahoma or southern Kansas RMT. Dashed grey line is the function $y = x$. Dotted grey lines are offset from $y = x$ by $10°$.
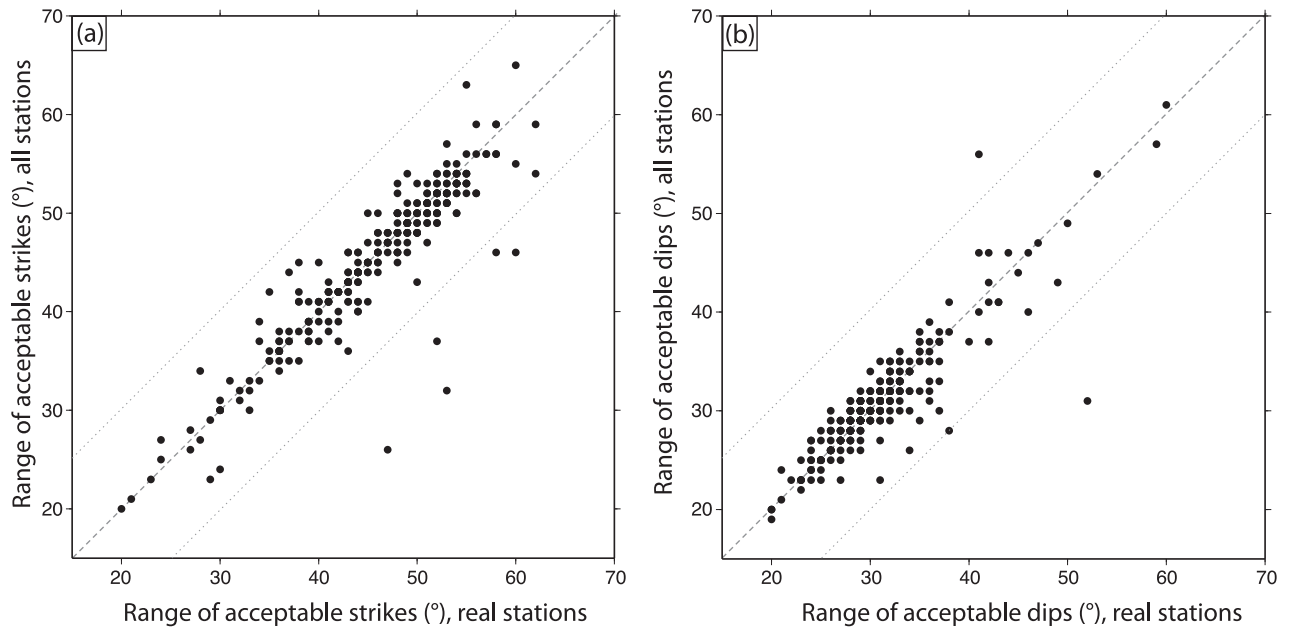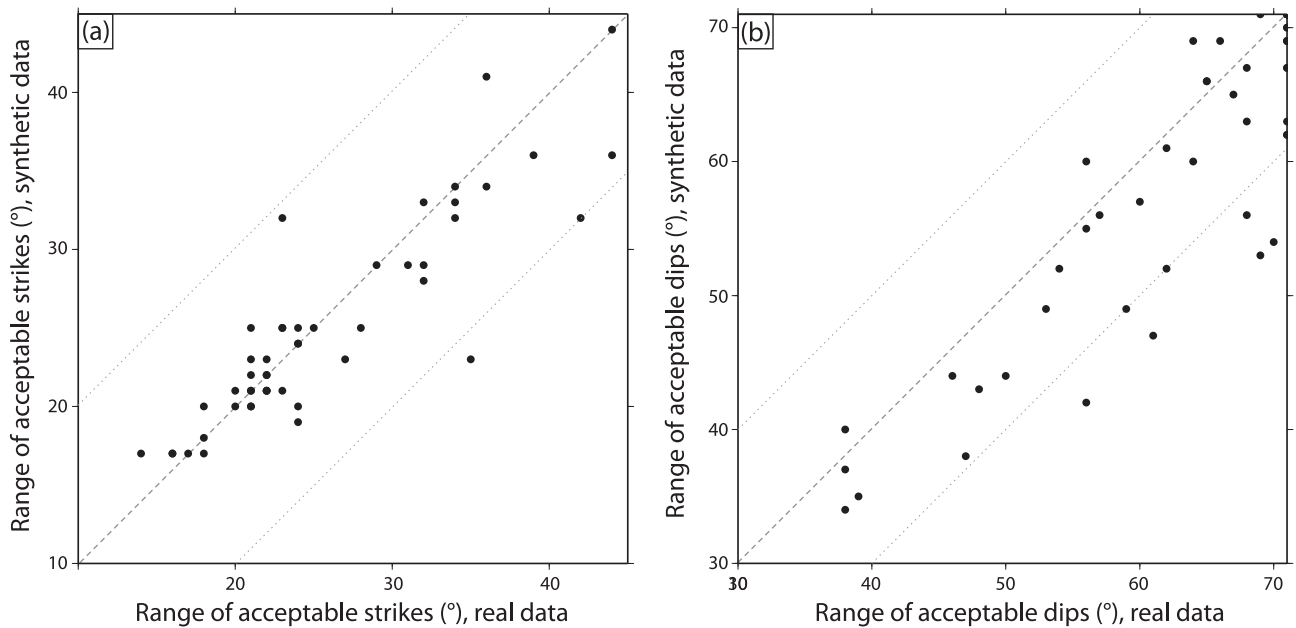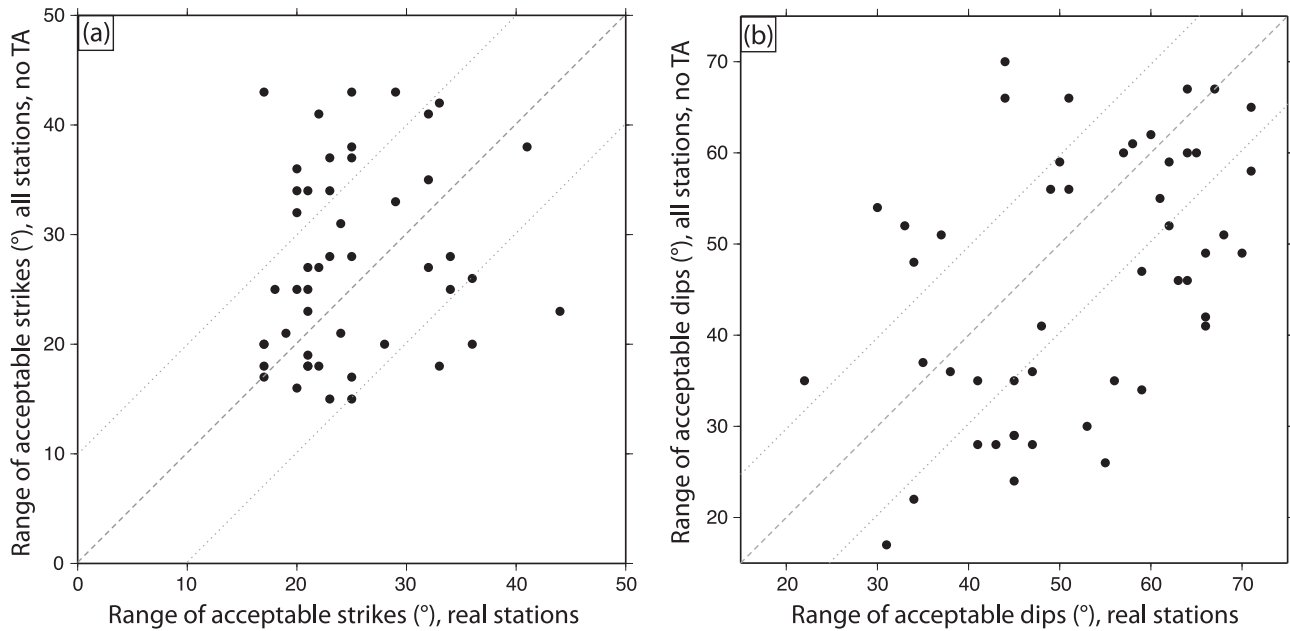
Figure A11. Range of acceptable (a) strikes and (b) dips using synthetic data with noise for stations used in the real inversion plotted against those computed when all central and eastern U.S. network stations were used (except the Transportable Array). Each black dot represents an individual RMT. Dashed grey line is the function $y = x$. Dotted grey lines are offset from $y = x$ by 10°.

APPENDIX B: SYNTHETIC SEISMOGRAMS FOR HYPOTHETICAL FOCAL MECHANISMS AND NETWORKS

We produced synthetic seismograms using Generic Seismic Application Computing (GSAC, Herrmann *et al.* 2004) for a variety of network geometries and two consistent focal mechanisms: (1) a M_W 4.0 earthquake occurring at 20 km depth with a strike, dip and rake of 0°, 45° and 90° (i.e. a pure dip-slip event); and (2) M_W 4.0 earthquake occurring at 5 km depth with a strike, dip, and rake of 315°, 90° and 0° (i.e. a pure strike-slip event). Because these tests use purely hypothetical data, no noise was added to the synthetic seismograms. We varied the following characteristics of network geometry and observe the effects on sensitivity:

(1) *Event-station distance*: Four stations at azimuths of 0°, 90°, 180° and 270° are placed at an equal distance from the epicentre. Six tests are conducted, with distance set to 25, 50, 100, 200, 400 and 600 km, respectively.

(2) *Azimuthal coverage*: Four stations are placed at 200 km from the epicentre and distributed evenly over limited azimuthal ranges, with the first station placed at 0°. Tests are conducted for five azimuthal ranges: 45°, 90°, 120°, 180° and 270°. In practice, coverage of 270° is identical to full coverage, since the stations are separated by 90° and a station is placed at due north (0° or 360°).

(3) *Event-station azimuth*: The four stations in (1) at a distance of 200 km (chosen for realistic proximity of earthquakes of the Maule and Oklahoma sequences to their respective stations) are repositioned with respect to the strike of the focal mechanism. The entire system is rotated 30°, 45° and 60° clockwise from the orientation in (1).

(4) *Network density*: Stations are placed at 200 km from the epicentre and distributed evenly azimuthally. Tests are conducted for five hypothetical networks: with 3, 4, 12, 24 and 36 stations.

B.1 Event-station distance

We demonstrate the impact of increasing station distance to the epicentres of dip-slip and strike-slip focal mechanisms, as described in Section 2A. In the first test, stations are 25 km from the hypocentre; distance is then increased to 50, 100, 200, 400 and 600 km. (Figs A1e and f).

For the reverse focal mechanism, dip is generally better constrained than strike. Dip is best constrained when stations are closest to the earthquake epicentre; uncertainty spans a range of just 12° when stations are at a distance of 25 km. As stations move farther away the range of acceptable dips increases, reaching 26° at 100 km station distance. The uncertainty range is relatively stable beyond 100 km (Fig. A1b). Strike sensitivity is much less variable than dip sensitivity, with a range of acceptable values between 30° and 36° for the distance ranges tested here. In this case, the range is largest (36°) when source-station distances are 25 km, decreasing slightly at distances of 50 km and larger, to a minima at 100 and 400 km (of the tested distances) with a range of 30° (Fig. A1a).

The range of acceptable strike is the same for stations at 100 and 400 km from the earthquake epicentre despite the different take-off angles of the first arrivals (computed using TauP, Crotwell *et al.* 1999) for these source-station distances. The stations plot at different distances from the centre of the focal sphere, with those at 100 km plotting very close to the edge of the focal sphere while those at 400 km plot closer to the centre (note that for a source-station distance of 25 km, the first arrival is specifically the upgoing compressional wave; for all other source-station distances, it could be either upgoing or downgoing). Interestingly, the source-station distances that have comparable takeoff angles to these optimal distances (50 km for the 100 km stations and 600 km or 25 km for the 400 km stations; Fig. A1f) do not have the same ranges. The same is true for dip: despite stations for source-station distances of 25, 50 and 100 km all plotting very near the edge of the focal sphere, their ranges of acceptable dip are 12°, 20° and 26°, respectively. This

quality of RMT sensitivity points to the importance of utilizing the full waveform in moment tensor inversions of dip-slip mechanisms; stations farther from the earthquake epicentre are subject to more seismic phases, lending in some cases to more complex waveforms.

For the strike-slip focal mechanism, we observe opposite tendencies of the reverse focal mechanism: strike is better constrained than dip (Figs A1c and d, respectively). Strike is very well constrained for most station-distance combinations, averaging a range of acceptable fits of ~10°. For this pair of northwest–southeast and southwest–northeast striking nodal planes, first arrivals plot centrally azimuthally in each of the four quadrants on the focal sphere (Fig. A1f). However, when stations are 25 km from the source, the range increases to 18°. RMT solutions are much less sensitive to change in dip than to change in strike at all source–station distances. Stations at distances of 100 and 200 km yield the smallest range of acceptable fits (25° and 27°, respectively), while the farthest and closest stations at 600 and 25 km yield the largest range of acceptable fits (53° and 49°, respectively).

It is interesting to note the opposite tendencies of strike and dip sensitivity to station distance for both mechanisms. Of the sampled distances for the reverse mechanism, strike is least sensitive at 25 km—the smallest distance—while dip is most sensitive at this distance. Similarly, strike is best constrained by stations at 100 km distance, which for dip is among the most poorly constrained distances. For the strike-slip mechanism, both strike and dip are poorly constrained by stations at 25 km. However, strike is better constrained by stations at all other tested distances, while stations at medial distances best constrain dip; the farthest stations provided the worst constraints on dip. This quality of network geometry suggests the importance of placing stations at variable distances from the seismic region, especially in tectonic regions where dip-slip faulting is anticipated.

B.2 Azimuthal coverage

Our tests with varying azimuthal coverage are similar to the event-station azimuth tests in that they introduce asymmetry to the fit fall-off curves. This asymmetry is more apparent in the strike sensitivity curves (Figs A2a and c) than in the dip sensitivity curves (Figs A2b and d). In analysing the fit falloff for previous tests, we suggested that symmetric curves depended on a station aligned with due north from the source; however, a station is fixed at due north for each case in this test, yet the strike and dip sensitivity curves are still asymmetric. We attribute this to uneven station distribution about due north (i.e., there are more stations in the clockwise direction than the counter clockwise direction). On the other hand, the results here are consistent with all prior tests in that the original station geometry (four stations separated by 90°) with the smallest azimuthal gap best constrains both mechanisms and both faulting parameters.

For the reverse mechanism, strike is less sensitive when the nodal planes are rotated counter-clockwise (negative delta) for all cases except the original station geometry (Fig. A2a). As strike rotates counter-clockwise, the strike of at least the north-striking nodal plane moves away from where first motions plot on the focal sphere, and thus the stations are only able to constrain changing strike in the positive-delta direction. Although for counter-clockwise rotations of strike the south-striking nodal plane is rotating towards some stations, there is still a large gap between the strike of the nodal plane and the azimuth of the first station for the three cases with poorest azimuthal coverage (Fig. A2f). In general, as azimuthal gap decreases, fit asymmetry decreases and strike constraint improves.

There is one exception to this trend: when 90° of the focal sphere are covered, strike is better constrained than when 120° are covered. We attribute this to the station positioned along the same azimuth towards which the north-striking nodal plane is dipping; consistently throughout these purely hypothetical tests, a station positioned at an azimuth of 90° has improved strike constraint.

Dip sensitivity for the reverse mechanism is affected by azimuthal coverage of the focal sphere in a very simple way: more complete coverage yields better-constrained dip (Fig. A2b). The asymmetry in the dip fit fall-off curves is subtle, affecting the range of acceptable fits by less than 1° for all cases.

Strike sensitivity for the strike-slip mechanism exhibits the same trends as those for the reverse mechanism. Strike is best constrained by the original station geometry, and asymmetry of the fit fall-off curve increases when azimuthal coverage decreases (Fig. A2c). Again, there is lesser asymmetry for 90° coverage than for 120° coverage. 90° coverage positions stations that symmetrically straddle one nodal plane for the best-fitting solution (Fig. A2f). The fit fall-off curve for 90° coverage closely resembles that for 180° coverage, but with a 1°-larger range of acceptable strikes. The 180° coverage improves upon the 90° network by positioning stations that straddle two nodal planes, though for this hypothetical focal mechanism the positions are not perfectly symmetrical about the nodal planes. These results support our earlier point that for strike-slip mechanisms, strike constraint is improved when sampling more quadrants of the focal sphere.

Dip sensitivity for the strike-slip mechanism follows a less distinguished trend compared to the other parameters in this test (Fig. A2d). Like the other parameters, the best-constrained case is still the original station geometry, and 90° coverage is second best (though the range of acceptable dips increases by 16°); however, the remaining three tests do not follow any obvious trend. After 90° coverage, 45° coverage provides the next-best constraint on dip. We attribute this to the station density; once the dip of the nodal plane changes enough to intersect with a first motion plotted on the focal sphere, causing significant changes in shape to the waveforms at that station, it also rapidly approaches the other first motions and changes those waveforms as well. This is not the case for 120° coverage, which yields the worst constrained dip.

B.3 Event-station azimuth

Each of the distance tests yields results that are symmetric about an angle change of zero ('delta-0'). For the reverse mechanism, this is in part because in each test two stations are aligned with the synthetic solution's nodal planes, while the first arrivals plot centrally within in each quadrant of the focal sphere for the strike-slip mechanism. In reality, aligning stations azimuthally with a fault's nodal planes is not simple; the precise strike of the fault may not be know during deployment, and geography and geology may not allow for ideal station locations. In light of this, we test how strike- and dip-sensitivity are affected when seismic station distributions are not aligned with our nodal planes (Fig. A3).

For the reverse mechanism, both strike and dip are best constrained when stations are positioned azimuthally parallel and perpendicular to the nodal planes; acceptable strikes have a 33° range and dips 25°. As with the distance tests, strike and dip sensitivity are affected differently when the orientation of the seismic network is rotated about the earthquake epicentre. Dip uncertainty distributions remain symmetric about the best-fitting solution (delta-0°), and at the tested orientations (30°, 45°, and 60°; Fig. A3e) the

range of acceptable solutions increases almost identically, to ~32° (Fig. A3b). Strike, however, is much more sensitive to this change in network geometry. The range of acceptable fits increases to >50° for all tested orientations, and is asymmetric for rotation angles other than 45° (Fig. A3a). Additionally, the change in relative fit becomes almost negligible in one direction. When the network is rotated clockwise by 30°, the relative fit stays well above 0.9 as the nodal planes are rotated clockwise. For the tested focal mechanism, first arrivals for the four stations provide poor coverage of the tensional and compressional quadrants (Fig. A3f). In most cases within the parameter space, two or more of the stations plot on or very near the nodal planes. This can be visualized by considering the station locations in Fig. A1(f) not only as rotated seismic networks, but also as the relative positions between the nodal planes and stations when the strikes of the nodal planes are changed. For example, the four-station network rotated clockwise 30° (Fig. A3f, top, second from the left) also shows the positions of the stations in their initial geometry (the first station at 0°) relative to the nodal planes, when the strike of the nodal planes is delta −30°. This quality highlights the importance of having stations in azimuthal alignment with dip-slip focal mechanism nodal planes, in order to sample at least one quadrant of each type (T or P) at some distance from the nodal plane. While this is difficult to achieve in *a priori* network deployments, it is most realizable for dense distributions of stations evenly spaced azimuthally about a target source zone.

The strike and dip fit falloffs for a strike-slip mechanism are similar in trend to those for the reverse mechanism (Figs A3c and d). The range of acceptable fits for dip remains symmetric about delta-0° for all orientations of the four-station network, with a range of 27° when a station is located due north and more than doubling to >60° for all other orientations (Figs A3d and e). Interestingly, the smallest range of acceptable fits coincides with a station at due north for both focal mechanisms, despite the 45° difference in strike of the nodal planes. This is likely because for the original station geometry, first arrivals plot more centrally azimuthally within each quadrant (for the initial focal mechanism) than for other orientations of the four-station network (Fig. A3f). Strike sensitivity follows the same trends for the strike-slip mechanism as for the reverse mechanism, but yields significantly different ranges of acceptable fit (Fig. A3c). Strike is very well constrained when a station is located due north, with a 9° range of acceptable fits. The sensitivity curve is still symmetric when the network is rotated by 45°, but the range of acceptable fits increases to 43°. When the network is rotated clockwise by 30° and 60°, the fit falloff becomes asymmetric, yielding acceptable fits spanning 13° in one direction but hardly changing relative fit in the other. Again, these ranges and characteristics of symmetry are likely due to the distribution of stations' first arrivals among the four quadrants of the focal sphere; first arrivals are more centrally located within the quadrants when a station is due north, which yields the tightest range of acceptable strike values. This is contrary to the trend of strike sensitivity for the reverse mechanism, where the smallest range of acceptable fits coincides with the station orientation that aligns with the nodal planes.

To constrain strike, the optimal orientation of this evenly distributed four-station network is the original station geometry, where the first station is located due north. This observation holds for both tested focal mechanisms, despite a 45° rotation between the strike of their nodal planes, and points to the potential importance of sampling the focal sphere quadrants at some distance from the nodal planes. This is accomplished differently for moderately dipping dip-slip faults than steeply dipping strike-slip faults.

B.4 Network density

As with distance tests, we find that each network density test produces uncertainty distributions that are symmetric about the best-fitting solution, delta-0°; again, this may be largely due to our choice to align the 'first' station at a due north azimuth (Fig. A4f).

In general, for both mechanisms, as network density increases, so does range of acceptable strikes and dips. This result is initially surprising, as intuitively more data providing more complete coverage should result in higher certainty; however, because all stations in this test are equidistant, they are weighted equally in the inversion and thus more stations mean each has a lower influence on the final computed fit. In other words, when many stations are used, the effects of those stations with poor fits to any combination of strike, dip, and rake in the grid search are balanced by other stations that maintain good fits.

There is one exception to the trend of increasing range with increasing station density for both strike and dip: both parameters are better constrained by four stations than by three. Using four stations, strike has a 34° range for the reverse mechanism and 8° range for the strike-slip mechanism (Figs A4a and c), while dip has 24° and 26° ranges (Figs A4b and d); other station densities have >42° and >28° for strike and dip, respectively, for the reverse mechanism, and >16° and >52° for the strike-slip mechanism. This is more likely a shortcoming of the three-station network than an advantage of the four-station network, since the 12-, 24- and 36-station networks have stations positioned in all the same locations as the four-station network (Fig. A4f).

APPENDIX C: COMPLETE ANALYSIS OF REAL AND SYNTHETIC SEISMOGRAMS FOR OBSERVED FOCAL MECHANISMS AND STATION DISTRIBUTIONS (SCENARIOS 1 AND 2)

C.1 Test case: M_W 8.8 Maule earthquake aftershock sequence

Ranges of acceptable strike for the real data (Fig. 3a) generally increase from east to west, perpendicularly to the shoreline. Ranges span from 9° to >71°, with a mean of 56° if those ranges >71° are assigned a value of 71° (we use this assignment throughout the analyses for both Chile and Oklahoma). Most earthquakes that occurred east of the shoreline have a range of acceptable strikes <50°, which is below the mean range of the data set. We suggest that this reflects that greater azimuthal coverage will yield an RMT with better-constrained strike. This is supported by our result from the synthetic azimuthal coverage tests (Appendix B), in which strike sensitivity for dip-slip earthquakes increases with azimuthal coverage. Also, the data for these onshore earthquakes include both small and large (i.e. less than and greater than 50 km) source-station distances, and thus variable take-off angles that provide better coverage of the focal sphere. The most poorly constrained aftershocks occurred at the southern bound of the data set, and those farthest offshore were especially poor. These epicentres have some of the largest azimuthal gaps within this data set, comparable to those reverse mechanisms with only 45° coverage in Appendix B, which also had very poorly constrained strikes. They differ from those at the northern end of the data set in two ways. First, the southernmost epicentres have roughly the same latitude as the southern extent of the IMAD network, so azimuths farther south are not covered; on the other hand, the IMAD network extends farther north than

the included aftershocks. Second, the coastline strikes at ∼30°, and infringing a 30° azimuthal gap north of the epicentre that is not filled in by stations farther south. Additionally, most of the aftershocks have best-fitting strikes that trend near-parallel to the coast and have nearly pure dip-slip mechanisms; thus, the azimuthal gap likely contains the strikes of both nodal planes. Discrepancies in range of acceptable strike among closely spaced epicentres likely result from noisy data, poor coverage of the focal sphere due to eliminated traces (addressed in the next section), and difference in mechanism and depth. Discrepancies of this sort also appear in other contour plots in this study.

The synthetic data (Fig. 3b) yield much smaller ranges of acceptable strike than the real data, spanning 20–62° with an average range of 46°. However, the trends observed in this plot generally agree with those for the real data. Range of acceptable strike increases from east to west, many of the best-constrained RMTs are on or near shore, and those with the worst constraint are far offshore and towards the southern end of the data set.

Fig. 3(c) compares the strike constraint of our real RMTs with that computed for synthetic waveforms with well-behaved noise. The plot shows the difference between Figs 3(a) and (b): the gridded ranges of acceptable strike for synthetic data with noise subtracted from the gridded ranges for real data. Appendix E compares the pure range values for each event. These values span the range −10° to 50°. The ranges of acceptable strike for the real onshore RMTs are closely matched by those for the synthetic RMTs, yielding difference values mostly 15° or smaller. The difference values generally increase to the west–northwest, as the ranges for real and synthetic data do independently, especially for RMTs within the southern half of the region. We make two suggestions based on the persistence of this trend throughout the real, synthetic, and difference plots. First, based on the real and synthetic plots, the increasing range of acceptable fits offshore results from station geometry and not simply from data quality. We infer this from the qualitative agreement between the real and synthetic scenarios, and as mentioned earlier, the large azimuthal gaps for offshore RMTs yield ranges analogous to those derived in the purely hypothetical tests in main text Section 2 and Appendix B (large ranges for poor azimuthal distribution). Second, the data quality for the offshore events is lower than for the onshore events. We base this statement on the difference plot: the ranges of acceptable strike for real and synthetic offshore RMTs differ by larger values than for the onshore RMTs. This trend may correspond to the way we incorporated noise into the synthetic waveforms; there was a lower signal-to-noise ratio for the real data than we included in the synthetic data, especially for offshore events. The noise level in the real data could reasonably be larger for earthquakes farther offshore, for which waveforms must travel much farther to reach seismometers. Ray paths from offshore events also likely travel through a more complicated velocity structure, including both the subducting Nazca and overriding South America plates; thus, differences between the assumed 1-D velocity model and real structure will be greater. For the few earthquakes that have negative difference values, our RMTs that used real data are better constrained than the synthetic RMTs, implying we included more noise in the synthetic waveforms than existed in the real data.

Ranges of acceptable dip (Fig. 4a) follow many of the same trends as strike, but mostly have smaller variability, spanning from 18° to 71° with a mean of 44°. Again, the earthquakes with epicentres onshore have better constrained dip with ranges mostly less than 30°, supporting our hypothesis that greater azimuthal coverage paired with varying source-station distances improves constraint on RMT parameters. The RMTs with poorest constraint on dip have

epicentres offshore but near the coast at the southern end of the data set, again attributable to large azimuthal gaps; however, this trend is subdued compared to that for strike in Fig. 4(a). This hints that when constraining the dip of RMTs, instead of gaining most from stations near the nodal planes as with strike, we gain from station distribution within the quadrants of the focal sphere. (Note that at the source–station distances observed here, most stations plot near the edge of the focal sphere—see Figs A1–A4(f)—and so to be near the nodal planes, stations must be at the correct azimuth.)

Again, the synthetic data (Fig. 4b) yield smaller ranges of acceptable dip than the real data, spanning from 20° to 60° with a mean of 31° (13° lower than for real data). The trends observed for the real data generally persist here; the best-constrained RMTs are mostly onshore, and the southern RMTs west of the coastline but close to the shore are among the most poorly constrained. However, there is much less evidence for increasing range towards the west–northwest, farther offshore. This is perhaps due to the uniform way we accounted for noise in the synthetic data. Realistically, as for strike, waveforms from earthquakes farther offshore are likely affected by more noise sources than those that are closer to the network, since they travel farther, and distance amplifies inaccuracies in the assumed velocity model. The real data contain these error sources, whereas the synthetic data do not. The lack of increase in range for earthquakes farther offshore, with larger azimuthal gaps, is consistent with our observations from Section 2: azimuthal coverage only slightly affects range of acceptable dips, and does not do so linearly (larger gap does not independently imply less sensitivity).

Fig. 4(c) compares the spatial distribution of dip constraint of our real RMTs with those computed for synthetic waveforms with well-behaved noise. Appendix E compares the pure range values for each event. Differences span −10° to 40°. The trend of increasing range offshore to the northwest observed in the real data (Fig. 4a) is evident in the difference plot; the ranges of acceptable dip for the real RMTs near or onshore closely match those for the synthetic RMTs, yielding difference values mostly 10° or smaller. As for strike, the difference values generally increase to the west–northwest, as the ranges of acceptable dip do in Fig. 4(a), especially for RMTs within the southern half of the region. Again, this likely corresponds to the uniform way we incorporated noise into the synthetic waveforms. However, several outliers far offshore yield low or negative differences between the real and synthetic plots. These RMTs are also outliers in the real data (Fig. 4a), tending to have lower ranges of acceptable dip than the other offshore earthquakes. This suggests that the real waveforms for the most important stations—those that have waveforms that change rapidly with small changes in dip (which are also likely to be well-distributed throughout the four quadrants of the focal sphere)—had higher signal-to-noise ratios than we incorporated into the synthetic tests.

C.2 Test case: regional seismicity in Oklahoma and southern Kansas

Fig. 9(a) shows the spatial variation in range of acceptable strikes for Oklahoma RMTs computed using real data (note that these earthquakes cluster over only a small area compared to the monitoring stations, and so many stations are not visible; Fig. 7 shows the complete station distribution). These ranges span 14–44° with a mean value of 26°, values much smaller than for the 30° and larger ranges computed for the Maule aftershocks. The more azimuthally complete distribution of seismic stations about the earthquakes,

especially near the strikes of the nodal planes, and the larger variation in source–station distances, contribute to better-constrained strike for these RMTs. This result reflects the tendencies we observed in Section 2, where good azimuthal coverage of strike-slip earthquakes achieves a <20° range of acceptable strikes. The range generally increases from south to north with a few outliers. Two RMTs at 97.78° W 37.12° N (42° range) and 97.60° W 36.58° N (44° range) have among the largest ranges of acceptable strike. These RMTs correspond to earthquakes with a notable dip-slip component, suggesting that the observed station distribution provides strong constraint on strike for strike-slip focal mechanisms, but does not perform as well for dip-slip events.

Fig. 9(b) shows the spatial variation in range of acceptable strikes computed using synthetic waveforms with noise generated for source-station pairs in Scenario 1. The ranges now span 17–44° with a mean value of 25°. The mean value has decreased by only 1° relative to that computed for the real data, though the lower bound on range has increased by 3°. This indicates that for most RMTs, the noise we added to the synthetic seismograms compared to that in the real data, and also that we were able to constrain strike on the real RMTs as well as we could have under conditions of well-behaved noise.

The difference plot in Fig. 9(c) is dominated by near-zero values (−1° to 1°), further exemplifying this accomplishment (Appendix E compares the pure range values for each event). Two of the few outliers correspond to the dip-slip mechanisms which yielded larger ranges of acceptable strike in the real data inversions, as discussed above (Fig. 9a); this clarifies that focal mechanism/style of faulting does not independently control strike uncertainty for this station distribution. Alternatively, the stations or components necessary for constraining these dip-slip events could potentially suffer from low signal-to-noise ratio, but this subset of earthquakes contains too few examples of dip-slip events to draw a strong conclusion.

Fig. 10(a) shows the range of acceptable dips for the Oklahoma RMTs computed using real data. The ranges span from 38° to >71° (71° being the largest range possible given the parameter space tested) with a mean range of 60° and only six focal mechanisms with ranges <50°. The maximum span and mean range are much larger than those computed for the Maule aftershocks, contrary to our initial hypothesis that greater azimuthal coverage improves RMT constraint, but consistent with our observations of the synthetic and purely hypothetical tests in Section 2. While a range of 60° is quite large, considering possible dips between 0° and 90°, recall that the searched parameter space centres around the best-fitting RMT; since most of the earthquakes in this subset occur on steeply dipping planes, the dip-space ranges from ∼55° to ∼125°, for example, many of the acceptable solutions allow the fault to dip supervertically, or subvertically with the fault strike rotated by 180° (but with the fault blocks still moving in the same direction with respect to one another).

In general, the range contours in Fig. 10(a) trend west–northwest to east–southeast, and increase in value towards the northeast. Again, this trend somewhat contrasts our initial hypothesis that azimuthal coverage should improve RMT constraint, since station coverage generally increases from west to east (see Fig. 7). Most of the earthquakes in Fig. 10(a) with anomalously low ranges of acceptable dip correspond to dip-slip events, a significant result suggesting that style of faulting may impact dip sensitivity, an issue discussed below.

Fig. 10(b) shows the spatial variation in range of acceptable dips computed using the synthetic waveforms with noise for the real

source-station from Scenario 1. The ranges now span 22° to >71° with a mean value of 52°. The mean value decreased by 8° relative to that computed for the real data, suggesting that for most RMTs, the signal-to-noise ratio we assigned was lower than that which existed in the real data. Recall, however, that in our analysis of strike, we observed only a small change in mean range between the real and synthetic data sets. The contrasting results here could imply varying levels of noise among station components; those more important for constraining strike have higher signal-to-noise ratio than those necessary to constrain dip. We address this issue more carefully below. The spatial trend in the synthetic data (Fig. 10b) is rotated clockwise by 90° from the real data (Fig. 10a); here, the range of acceptable dips increases from northwest to southeast. Despite this rotation, the general pattern compares to that in the real data: the RMTs with the largest ranges are in the southeast, among good station density and azimuthal coverage, while those with the smallest ranges are in the northwest with less complete azimuthal coverage. This further supports our suggestion that the range of acceptable fits may depend not only on station geometry/azimuthal coverage, but also on faulting style.

Fig. 10(c) shows the spatial variation in difference between ranges computed for the real and synthetic RMTs. Section E compares the pure range values for each event. Here, the outliers—which only loosely follow a spatial trend—dominate the appearance of the contours. As in many of the other analyses, this contrast likely depends on the amount of noise added to the synthetic data compared to the real data quality. Nevertheless, we were able to resolve most of the RMTs using real data to a comparable level of constraint compared to those from synthetic data with well-behaved noise.

In order to better illustrate how faulting style impacts the range of acceptable dip, Figs 11(a) and (b) plot ranges for two groups of faulting events, divided based on rake. The earthquakes in Fig. 11(a) deviate in rake from pure strike-slip by <20°, while those in Fig. 11(b) deviate in rake from pure strike-slip by >20°, indicating a considerable dip-slip component. Importantly, all but one of the earthquakes in Fig. 11(b) occurred in the northwestern quadrant of the plot. This lends a tectonic implication – i.e., dip-slip (normal) faulting accommodates deformation in this region.

The strike-slip RMTs include 41 earthquakes with ranges of acceptable dip spanning 38° to >71° and a mean value of 64°; the dip-slip events, which include only 8 earthquakes, span 38° to 70° with a mean value of 50° (though only one has a range larger than 56°, which dominates the mean; when excluded the mean drops to 50°). Qualitatively, the difference in ranges is easy to see in Fig. 11. Both plots are coloured using the same colour scale and follow the trend of increasing range from southeast to northwest; however, the contours in Fig. 11(b) are shifted northeastward compared to those in Fig. 11(a), indicating lower ranges of acceptable dip for RMTs with closely spaced epicentres but a dip-slip component. This cautions us to consider faulting style when analysing trends in the range of acceptable dips, rather than station distribution alone.

APPENDIX D: EFFECTS OF THE TRANSPORTABLE ARRAY ON RMT SENSITIVITY

Because the Transportable Array (TA) is a unique case with very specific station geometry, we did not include TA stations in the Scenario 3 Oklahoma and southern Kansas test case analyses in the main text. Here, we include an additional scenario, Scenario A1, to demonstrate how including the TA stations impacts the ranges

computed for each RMT parameter. (*Note:* there are 32 TA stations within 300 km of the study area, close enough to receive full weighting, and 119 within 600 km, the cut-off distance to potentially be included in the inversion.)

The ranges of acceptable strike span comparable values whether TA stations are or are not included: Scenario A1, with TA, spans 15° to 54° (though only one earthquake has a range larger than 43°) with a mean value of 28°; Scenario 3, without TA, has the same range and mean. The TA stations have little impact on the computed ranges. Figs A5(a) and (b) show the spatial variation among the ranges computed for Scenarios A1 and 3, respectively. Fig. A6(a) plots the ranges computed when TA stations were included against those computed without the TA stations. This plot closely follows the function $y = x$, with a few points straying from the line by up to 3°. This is perhaps because the TA stations constrained only the eastern side of most RMTs, and only limited distances on the western side of those RMTs that were located within the bounds of the TA stations; furthermore, although there were many TA stations within 600 km of the aftershock epicentres, only 32 were within distances weighted most strongly in the RMT inversion process.

Like strike, the ranges of acceptable dip span comparable values whether TA stations are or are not included: Scenario A1, with TA, spans 17–68° with a mean range of 46°, while Scenario 3, without TA, spans 17–70°, also with a mean range of 46°. Again, the TA stations have little impact on the computed ranges. Figs A7(a) and (b) show the spatial variation among the ranges of acceptable dip computed for Scenarios A1 and 3, respectively. Fig. A6(b) plots the ranges computed when TA stations were included against those computed without the TA stations. Like for strike, this plot closely follows the function $y = x$, with only a few points straying from this line and by only as much as 2°.

APPENDIX E: QUANTITATIVE COMPARISON OF COMPUTED RANGES OF ACCEPTABLE STRIKE AND DIP

E.1 Test case: M_W 8.8 Maule earthquake aftershock sequence, Scenarios 1, 2 and 3

Fig. A8(a) compares the ranges of acceptable strikes computed in Scenarios 1 and 2 (i.e. ranges computed using real data against ranges computed using synthetic data with noise, but for the real station locations) for each RMT computed for a Maule aftershock included in this test case; Fig. A8(b) shows the same for dip. For both parameters, the majority of data points plots below the line $y = x$, indicating that most events were better constrained by Scenario 2; in other words, the real data were noisier than we accounted for in the synthetic data. However, ~6 per cent of the RMTs were better constrained by the real data, in which case we included more noise in the synthetic data than was present in the real data. The ranges obtained for each scenario differ by <10° for roughly half the RMTs for each parameter. These results are consistent with the spatial trends observed in the main text.

Fig. A9(a) compares the ranges of acceptable strikes computed in Scenarios 2 and 3 (i.e. ranges computed using synthetic data with noise for only stations used in the real RMT inversion against ranges computed when all IMAD stations are used); Fig. A4(b) shows the same for dip. For both parameters, roughly half of the RMTs are better constrained when all stations are used (the data plots above the line $y = x$), while the other half are better constrained (plot below $y = x$) by the station combination used for the real

inversion. This result is consistent with our observations Appendix B: increasing station density does not necessarily improve strike and dip constraint. However, for both parameters, the ranges computed for Scenarios 2 and 3 are consistent to within 10° for all but a few RMTs (five and two for strike and dip, respectively). This suggests that for this network geometry and set of focal mechanisms, the trade-off between adding addition stations and maintaining RMT constraint is small.

E.2 Test case: regional seismicity in Oklahoma and southern Kansas, Scenarios 1, 2, 3 and A1

Fig. A10(a) compares the ranges of acceptable strikes computed in Scenarios 1 and 2 (i.e. ranges computed using real data against ranges computed using synthetic data with noise, but for the real station locations) for each RMT computed for an Oklahoma or southern Kansas earthquake included in this test case; Fig. A10(b) shows the same for dip. For dip (Fig. A10b), most data points plot below the line $y = x$, indicating that most events were better constrained by Scenario 2, and that like the Maule test case, we may have included less noise in the synthetic data than was present in the real data. However, strike was better constrained by the real data for ~12 per cent of the RMTs, and for these events we may have included more noise in the synthetic data than was present in the real data. The ranges obtained for each scenario differ by <10° for almost 90 per cent of RMTs for strike. These results are consistent with the spatial trends observed in the main text. Strike constraint (Fig. A10a), however, follows a different pattern. About half the data points are better constrained by the real data than the synthetic data with noise; we address this in the main text.

Fig. A11(a) plots the ranges of acceptable strike for Scenario 2 against Scenario 3 (synthetic data for the stations used in the real inversion against those ranges computed when all stations are used); Fig. A11(b) shows the same for dip. For strike (Fig. A11a), most points plot above the diagonal $y = x$, corresponding to RMTs with strikes better constrained by fewer stations; however, about one third of the events plot below the line, thus demonstrating better constraint with more stations. The opposite is true for dip (Fig. A11b), in which about one third of the events plot above the line, indicating better constraint by fewer stations, while the rest are better constrained by more stations. In both cases, there is significant scatter among the plots, and many RMTs are outside of the 10° bounds that include most events for other scenarios and test cases. This suggests that for these focal mechanisms and station geometry, RMT sensitivity is highly dependent on station selection.

APPENDIX F: EVALUATION OF INDIVIDUAL STATION COMPONENTS WITH CHANGING DIP FOR THE FOUR-STATION NETWORK

The four-station network yields three results that contrast all other tests. First, all other tests produced ranges of acceptable strike smaller than their respective ranges of acceptable dip, yet this hypothetical four-station network produced the opposite. Second, the transverse component constrained dip better than the radial and vertical components, yielding the smallest range of acceptable dips of all the test cases. The radial and vertical components for the four-station network yielded the largest ranges of acceptable dip of all the individual component tests, at a range of 29°. Third, the

radial and vertical components provide poor constraint on strike, with a range of acceptable strikes $> 70°$. We focus on the third result, as the four-station network is the only test case in which strike was not constrained within the parameter space. We speculate that this results from the position of the stations relative to the nodal planes throughout the parameter space. Because the stations in the four-station network plot centrally between the two nodal planes for this focal mechanism—45° from the strike of each—and our parameter space extends only 35° in each direction from the best-fitting strike, neither nodal plane ever crosses a station on the focal sphere (note that the four-station network is our only test case in which this occurs). Thus, the waveform polarity is consistent for the duration of the time-series for all values of strike; as a result, the misfit between the waveform of the best-fitting strike and that for each rotation of strike cannot exceed the amplitude of the waveform for each time sample. Because waveforms by nature intersect the x-axis numerous times, these nodes of intersection and the surrounding points have very small misfits compared to the larger amplitude data points.

Additionally, as time increases and waveform oscillations decrease in amplitude, maximum misfit is further limited. These qualities may therefore be hampering the ability of our RMT inversion method, which weights each time sample of the waveforms equally, regardless of amplitude or time elapsed since the *P*-arrival. When we increase station density (or, alternatively, use only three stations), we ensure that the waveform for at least one station will change polarity for some delta-strike within our tested parameter space, and consequently will decrease the range of acceptable fits.

Waveforms recorded by the transverse component behave differently from the radial and vertical components, stretching or shortening in addition to changing amplitude when strike rotates away from the best-fitting plane. This quality of the transverse component allows the RMT conversion to better distinguish between waveforms that characterize source mechanisms with varying strikes. Thus, when the inversion uses only the transverse component as input data, the computed data-model fit value is very sensitive to changing strike, yielding only a 1° range of acceptable strikes.